Wind-stress simulations and equatorial dynamics in an AGCM
Part I: Basic results from a 1979-1999 forced SST experiment

Julio T. Bacmeister

Goddard Earth Sciences and Technology Center University of Maryland, Baltimore County, Baltimore, MD 21250, and
NASA Seasonal-to-Interannual Prediction Project, NASA GSFC, Greenbelt, MD 20771

Max J. Suarez

NASA Seasonal-to-Interannual Prediction Project, NASA GSFC, Greenbelt, MD 20771

Abstract. This is the first of a two part study examining the connection of the equatorial momentum budget in an AGCM, with simulated equatorial surface wind stresses over the Pacific. The AGCM used in this study forms part of a newly developed coupled forecasting system used at NASA's Seasonal-to-Interannual Prediction Project. Here we describe the model and present results from a 20-year (1979-1999) AMIP-type experiment forced with observed SSTs. Model results are compared them with available observational data sets. The climatological pattern of extra-tropical planetary waves as well as their ENSO-related varibility is found to agree quite well with re-analysis estimates. The model's surface wind stress is examined in detail, and reveals a reasonable overall simulation of seasonal interannual variability, as well as seasonal mean distributions. However, an excessive annual oscillation in wind stress over the equatorial central Pacific is found. We examine the model's divergent circulation over the tropical Pacific and compare it with estimates based on re-analysis data. These comparisons are generally good, but reveal excessive upper-level convergence in the central Pacific.

In Part II of this study a direct examination of individual terms in the AGCM's momentum budget is presented. We relate the results of this analysis to the model's simulation of surface wind stress.

1.Introduction

Coupled atmosphere/ocean forecasts of sea-surface temperature variability in the Equatorial Pacific are a promising avenue to obtain predictions of climatic conditions over large parts of the Earth months or even years in advance. However, such forecasts remain a vexing problem because they involve interannual, seasonal and perhaps synoptic modes of variability in the ocean and atmosphere. The performance of coupled, atmosphere/ocean, general circulation models (CGCMs) may be adversely affected by biases in either the atmospheric (AGCM) or oceanic (OGCM) component. Accurate simulation of equatorial ocean wind stresses in AGCMs presents a particular challenge since momentum forcing terms are weak.

The present study was motivated by atmospheric model development efforts at NASA's Interannual-to-Seasonal Prediction Project (NSIPP). The major focus of NSIPP's research is to assess the impact of satellite-derived, sea-surface height data on fully-coupled atmosphere/ocean forecasts. An important part of this assessment are numerical simulations of ocean data impact on the coupled system. Given the uncertainty concerning the degree of interaction between seasonal and interannual modes in the ENSO phenomenon, such simulations are ideally performed using a CGCM with realistic variability at both seasonal and interannual time-scales.

Figures 1 and 2 show the time-mean and seasonal cycle of wind-stress taken from an atmosphere-only experiment using a previous version of our AGCM. Figures 1 and 2a show results from an experiment in which this version of our AGCM was forced with observed SSTs for 1979-1999 (an "AMIP-type" experiment). A comparison with COADS estimates of actual wind stress reveals numerous shortcomings. The time-mean stress is too strong by about 30% and the amplitude of the model's seasonal cycle is strong as well (c.f., Figs. 2a,b). There is a strong semi-annual component in the model cycle east of 150W that is not present in the observations. The peak westerly anomaly in March is too far west, and the overall pattern of anomaly evolution does not

1

exhibit the propagating character seen in the observations. When this version of our AGCM was coupled to our Ocean GCM [Schopf and Logue, 1995; Yu and Schopf, 1997], the problems evident in the AGCM wind-stresses appeared to have an impact on the simulated SST evolution in the CGCM, as can be seen in Figures 2c. Compared with observations of SST (Fig. 2d), the CGCM produces a highly distorted seasonal cycle in the EEP, with excessive semi-annual variation.

The current version of our AGCM (hereafter referred to as the NSIPP-1 AGCM) was developed in an attempt to alleviate the deficiencies in equatorial wind stress evident in Figures 1 and 2, as well as, other deficiencies in the simulation of tropical precipitation and extratropical planetary wave ENSO response. Improvements in these areas were sought not only for improved coupled model performance, but also for improved "Tier 2" seasonal forecasting, that is atmospheric forecasts using prescribed SSTs [e.g., Shukla et al., 2000]. The important model changes undertaken to complete NSIPP-1 included increasing the vertical resolution in lower troposphere, and modifying turbulence, convection, and cloud parameterizations. A more complete description of the current model is given in Section 2.

In this two-part study, we will examine in detail the behavior of the NSIPP-1 AGCM in the tropics and its relation to model simulations of seasonal and interannual variations in surface wind stress. Part I will present wind-stress, precipitation, and planetary wave simulations, as well as analyses of divergent flow in a 20-year AMIP run using NSIPP-1. Model results will be compared with NCEP/NCAR re-analyses [Kalnay et al., 1995], CMAP precipitation climatologies [Xie and Arkin, 1997], and surface wind stress climatologies from SSMI [Wentz, 1997] and COADS [Da Silva, 1994]. We will focus on isolating seasonal and interannual modes of variability in the model results. In Part II [Bacmeister and Suarez, 2001], we examine in more detail the dynamics of the equatorial atmosphere in the model, and how these contribute to the model's simulation of wind-stress over the eastern equatorial Pacific (EEP). This is done, in

part, by peforming a term-by-term analysis of the model's zonal momentum budget near the Equator. A particular focus of Part II will be to separate the contributions of deep-tropospheric dynamics [e.g., Gill 1980, etc] dynamics and shallow boundary-layer dynamics [e.g., Lindzen and Nigam, 1987] to simulated wind-stress variability in the EEP.

Relevant aspects of the NSIPP-1 AGCM are described in Section 2. In Section 3, we show results of the 20-year (December 1979-December 1999) AMIP simulation using NSIPP-1. First, upper-air fields and precipitaion are shown in Section 3.1. The mean, interannual and seasonal behavior of surface wind stresses in the model is examined in Section 3.2. In Section 3.3 we analyze the model's divergent circulation. This includes an examination of localized, zonal and meridional circulations [Trenberth et al., 2000] in addition to the better-known Walker and Hadley cells. Finally in Section 4, we summarize the results of Part I.

2. Model Description

The dynamical core of the NSIPP-1 AGCM has been fully described in Suarez and Takacs (1995). NSIPP-1 is a grid point model using the vector-invariant form of the momentum equation. A 4th-order Arakawa Jacobian with explicit leapfrog time differencing is used to integrate the momentum equations. Prognostic equations .for moisture and potential temperature are integrated using a 4th-order space centered flux formulation in the horizontal with leapfrog time-differencing. The vertical coordinate used in these experiments is a standard σ-coordinate and vertical differencing follows Arakawa and Suarez (1983). Vertical tracer-advection is accomplished using space-centered 2nd-order differences. An 8th-order Shapiro filter is used to dissipate small horizontal scales in all prognostic fields except surface pressure. A polar Fourier filter is applied poleward of 45° latitude to the time-tendencies of all prognostic variables. Below we briefly discuss the status of relevant physical parameterizations in the NSIPP-1 AGCM.

2.1 Resolution

The simulations described in this study were performed with a uniform horizontal resolution of 2° latitude by 2.5° longitude and 34 unevenly spaced σ-levels in the vertical. The distribution of these levels is shown in Table 1. We have found that our simulations of northern winter planetary wave patterns improve when filtered topography is used in place of the straightforward gridbox mean elevation. For the simulations presented here we have used topopgraphy that has been filtered using a 12th order "Coiflet" wavelet (Daubechies, 1992). To achieve this we simply take the 2D discreet wavelet transform of 2°x2.5°topography on the model's latitude-longitude grid. The transform amplitudes in the highest octaves (highest spatial frequency band) are zeroed, and the inverse transform is then performed. Since wavelets are localized functions, only small amounts of "ringing" occur. Coiflets are used because of their approximately symmetrical shape.

2.2 Boundary Layer and Surface parameterizations

The boundary layer scheme is a simple K-scheme, which calculates turbulent diffusivities for heat and momentum based on Monin-Obukhov similarity theory [Louis et al., 1982]. The surface exchange coefficients for momentum and heat are given by,

$$C_{m,h} = \left(\frac{k}{\ln \frac{z}{z_0}}\right)^2 f_{m,h}(\mathrm{Ri}, \frac{z}{z_0})$$

Where z_0 is the roughness length, k is the von Karman constant and Ri is a bulk boundary-layer Richardson number. Over oceans a uniform value of $z_0=2 \times 10^{-4}$ meters is used. Over land the value of z_0 depends on surface type (Koster and Suarez, 1992). The functions $f_{m,h}$ are derived from the universal Monin-Obukhov vertical structure functions for shear and stability. The definitions of C_m and C_h above are generalized to derive exchange coefficients between sigma layers according to,

$$K_{m,h} = \left(\frac{kz}{1 + \frac{kz}{\lambda_0}}\right)^2 |\partial_z \vec{u}| f_{m,h}(\mathrm{Ri}, \frac{z}{z_0})$$

Here λ_0 is a length scale which we take to be 20 m. This is lower than used in other implementations of this scheme. However, we find that the lower value used here results in much better simulations of oceanic wind stresses along the equator without degrading other aspects of the simulations. This low value of λ_0 may be compensating in part for excessive free-tropospheric pressure gradients in the model, which contribute to the generation of surface wind stress.

2.3 Convection

The NSIPP-1 AGCM uses the relaxed Arakawa-Schubert (RAS) scheme to parameterize convection [Moorthi and Suarez, 1992]. RAS uses a sequence of simple linearly-entraining plumes (cloud types) that originate and detrain at specific model levels. Each cloud type is characterized by an entrainment rate and a cloud-base mass flux. The characteristic entrainment rate is determined from the environmental stability

5

profiles to ensure that plumes originating at the desired cloud-base will lose buoyancy, or detrain, at the desired detrainment level. The number of possible cloud types is given by the number of allowed pairs of cloud base levels and detrainment levels. In our current implementation, all convection is assumed to begin in the lowest model level. However, convective clouds can detrain at any level above this, so that the number of possible cloud types is equal to the number of vertical levels minus one.

The initial mass flux for each cloud type is determined from a CAPE closure [Arakawa and Schubert, 1972], which, roughly speaking, specifies larger mass flux with increasing CAPE. RAS is called during each model time step, and during each call to RAS every cloud type is invoked sequentially, starting with the shallowest cloud. An adjustment time scale of 1800 seconds is assumed for clouds detraining above $\sigma=0.5625$ and a time scale of 900 seconds is used for clouds detraining below this level. Re-evaporation of convective rain is estimated using the approach of Sud and Molod (1988).

In our implementation of RAS, convection originates from the relatively-thin, lowest model layer ($\Delta\sigma=0.015$), and can detrain into any layer above. Thus, we are in effect allowing RAS to act as a parameterization of both deep and shallow convection in our model. It is not clear that the assumptions made in deriving RAS apply for shallow convection, e.g., small updraft areal fraction. Nevertheless, the model appears to be producing a reasonable simulation of the thermodynamic structure of the lower troposphere over the EEP. Our current implementation of RAS neglects downdrafts as well as convective momentum forcing (cumulus friction).

2.4 Large-scale clouds

Large-scale cloudiness is determined in two steps. First, an intial cloud fraction is estimated using a simple relative humidity based diagnostic scheme such as that of Slingo (1989). A high threshhold relative humidity of 95% is used. Even with this

high threshhold value, excessive cloudiness results over tropical and subtropical oceans. Thus, a second "destruction" step is invoked that uses the magnitude of subsidence drying produced by RAS to destroy a fraction of the large-scale clouds produced by the relative humidity diagnostic,

$$C_{ls} = \max\left[C_{ls}^* \left(1 - \left[\frac{D_{cnv}}{D_0}\right]^2\right), 0\right]$$

where C_{ls}^* is the initial estimate, D_{cnv} is the net convective drying from RAS due to all clouds affecting that layer, and D_0 is a tunable parameter, which we choose by examining the global radiation budget.

The large-scale cloud scheme also produces rain when the relative humidity exceeds 1.00. Large-scale rain is produced during each time step and is accumulated from the top down. Large scale rain falling into a gridbox from above is allowed to reevaporate to saturation before continuing to the next gridbox below.

2.5 Radiation

The parameterization of solar and infrared radiative heating used in the model is described in Chou and Suarez [1999] and Chou and Suarez [1994]. The solar heating includes absorption by O_3, CO_2, water vapor, O_2, and clouds as well as gaseous and aerosol scattering. The solar spectrum is divided into eight visible-UV bands and three near-IR bands. A k-distribution method is used within each band. The eight visible-UV bands use a single k-interval, while the near-IR bands use ten intervals each. Effects of multiple scattering by clouds and aerosols are treated using the δ-Eddington approximation for the direct beam and the Sagan-Pollock approach for diffuse radiation. The infrared parameterization allows for absorption by O_3, CO_2, water vapor, N_2O, CH_4, CFC-11, CFC-12 and CFC-22, within eight spectral bands, but for the results discussed here only O_3, CO_2, and water vapor are included.

3. AMIP Results

This Section examines results from a 20-year (December 1, 1979-November 31, 1999) AMIP-type experiment conducted using NSIPP-1. The experiment was initiated from NCEP re-analysis fields on December 1, 1978, but the first 12 months of the integration are not used in the present study. The experiment examined here is one of a set of 9 AMIP-type experiments recently completed with the NSIPP-1 AGCM. A detailed description of the model's 20-year (1979-1999) climatology can be found in Bacmeister et al. (2000), an atlas that compares seasonal mean fields from the model with various observational data sets.

3.1 Basic Model Climate

DJF Upper Air Fields. The simulation of boreal winter stationary planetary waves is an important indicator of general model performance. Also, the response of these waves to ENSO-related SST variations in the tropical Pacific is a key component in succesful dynamical seasonal prediction [Shukla et al., 2000]. Figure 3 shows simulated upper air fields for December-January-February (DJF). The boreal winter zonal wind and eddy geopotential height (Φ^*) at 200 mb averaged over the 20 seasons (1979-1999) compare well with NCEP re-analyses for the same period. The main problems with the simulation include an unrealistically strong westerly "saddle" over the EEP, and a westerly bias in the southern hemispheric mid-latitude jets. Upper tropospheric easterlies are too strong over Africa and too weak over the maritime continent. The minimum in (Φ^*) over the northeastern Asia is somewhat weak, while the high over western North America is too strong.

ENSO-related interannual variability is generally well simulated, as indicated in Fig. 4, which shows the difference between Φ^* for DJF 1982/83 and DJF 1988/89, years of strong warm and cold ENSO anomalies. The geopotential dipole pattern over the N. Pacific is well simulated in both shape and amplitude. This is associated with the

8

extension of the East Asian Jet across the Pacific during warm ENSO events. Over eastern N. America, the re-analysis shows more eastward elongation of the positive Φ^* anomaly associated with warm ENSO conditions. However, the degree to which these differences may be due to chaotic internal variability cannot be assessed from a single realization. Pegion et al. [2000] have analyzed ensembles of seasonal forecasts using NSIPP-1 and conclude that the model's ENSO response is statistically close to that obtained from re-analysis fields.

Overall, the simulation of upper-air fields in NSIPP-1 compares favorably with that of AGCMs in the AMIP project [Gates et al., 1999]. Zonally-averaged wind profiles and velocity potentials at 200 mb as well as sea-level pressure fields [Bacmeister et al., 2000] are close to the multi-model ensemble averages for all of these quantities. In the case of 200 mb zonal wind the NSIPP-1 profile is closer to re-analyses than the AMIP-project ensemble mean.

Precipitation. The model's 20-season climatological precipitation fields are also in generally good agreement with the observed fields (Fig. 5). The overall pattern and intensity of rain in the South Pacific convergence zone (SPCZ) during DJF is well captured. Wintertime midlatitude rain belts, or storm tracks, in the North Pacific and North Atlantic are also well simulated. During July-August-September (JAS) the model's climatological precipitation is less-satisfying, although the simulation is generally good. The northward shift in maximum precipitation over the western Pacific during JAS is captured. The weakening and westward shift of the SPCZ is also reasonably well reproduced.

However, some significant errors in the precipitation field are worth noting. There is a tendency for the ITCZ across the Pacific to "split" in both DJF and JAS, leaving the central Pacific (140W-110W) dry while the eastern Pacific close to Central America is too wet. During DJF (Fig. 5a) the model produces a concentrated area of strong precipitation immediately to the west of Mexico at around 12N. In the observations

(Fig. 5b) the same area is almost completely dry, with precipitation rates well below 1 mm d^{-1}. During JAS (Fig. 5c) this zone of precipitation expands and shifts further east so that it is actually positioned over land in Central America and Southern Mexico with strong precipitation rates extending well into the Caribbean. In the observations for JAS (Fig. 5d) there is strong precipitation over the eastern Pacific, but it is centered a few degrees further south $\approx$10N, and well to the east, with only weak precipation over the Caribbean. A similar model tendency to split the ITCZ is discernible over the tropical Atlantic.

Other notable model biases include the strong precipitation "bridge" connecting the Pacific ITCZ with the North Pacific storm track, evident just near 150W during DJF. Hints of such a feature are present in the observations, but with lower precipitation rates. There is excessive rainfall north of the Equator in the far western Pacific and Indian ocean during DJF. The model's Asian monsoon rainfall during JAS is too concentrated in the Bay of Bengal. Another monsoon related bias occurs over the western Indian ocean near the Horn of Africa, where the model produces a small area of intense precipitation that is absent from the observations.

Figure 6 illustrates the ENSO signal in the model precipitation. The figure shows anomalous precipitation for DJF 1997/1998, i.e, for strong El Niño conditions, and for JAS 1999, during strong La Niña conditions. The overall response of the model precipitation to these SST extremes is good. During El Niño conditions (Fig. 6a) the model's Pacific ITCZ and SPCZ appear to merge and shift eastward leading to anomalously dry conditions along the length of the climatological ITCZ (10N), near the Maritime Continent, and also in the climatological region of the SPCZ, a swath extending southeast from Indonesia to a point near 150W and 30S. The central and eastern Pacific (180-90W) along the Equator are much wetter than normal. These anomalies are in good agreement with observational estimates (Fig. 6b). During La Niña conditions (Figs. 6c and 6d) the model correctly simulates the westward shift

10

of maximum precipitation over the Western Pacific, which leaves anomalously dry conditions between 150E and 180. Also, the Pacific ITCZ (10N,150E-90W) is generally drier in both observations and model.

The simulation of precipitation in NSIPP-1 is excellent compared with that of the AMIP-project models [Lau et al., 1996; Gates et al., 1999]. The mean precipitation for northern summer is, generally-speaking, better than the ensemble mean for the AMIP-project models [c.f., Fig. 4a, Gates et al., 1999]. The AMIP-project ensemble shares our model's tendency to split the Pacific ITCZ, but, elsewhere, the NSIPP-1 precipitation is closer to the Xie-Arkin observation. In particular, precipitation over the W. Pacific warm-pool and Eastern Indian Ocean is stronger (and closer to observations) in our model than in the AMIP-project ensemble mean. In northern winter, the NSIPP-1 precipitation is also in better agreement with observations than the AMIP-project ensemble over most of the globe. A notable exception to this is the present model's large wet bias near 12N, off the coast of Mexico.

Equatorial cross-sections. Figures 7 and 8 show longitude-pressure sections of zonal wind u and potential temperature θ along the Equator. The model u cross-sections are generally similar to those from the NCEP re-analysis, particularly for DJF (Figs. 7a and 7b). The model's upper tropospheric westerlies between 100 and 300 mb in the western hemisphere tend to be too strong. During JAS (Figs. 7c and 7d) the agreement between model and re-analysis u is not as good. Discrepancies are largest over the central and eastern Pacific. In the upper troposphere over this region the model produces a complex pattern of alternating westerlies and easterlies with strong easterlies centered over 90W to 100W. Hints of such pattern are discernible in the re-analysis u, but are much less pronounced. In the lower troposphere between 180 and 120W, the model's seasonal variation in u is opposite to that in the re-analysis. Model easterlies in this region intensify during JAS, while re-analysis easterlies appear to weaken slightly, as is particularly evident around 850 mb. This behavior in the re-analysis u is interesting

11

in light of the fact that observed easterly wind-stress in this region strengthens during JAS, although not as much as our model's simulated wind stress (c.f. Section 3.2).

Equatorial cross-sections of θ in the model and re-analysis (Fig. 8) are also in good general agreement. Again the agreement appears somewhat better in DJF (Figs. 8a and 8b) than in JAS (Figs. 8c and 8d). During JAS the model θ-section exhibits generally upward sloping isentropes eastward from around 90E across the entire Pacific basin to 90W. In the re-analysis section isentropes attain their minimum altitude close to 130E and slope upward both to the east and to the west. In addition, the re-analysis θ suggests a somewhat deeper boundary layer over the EEP, during both seasons, than is present in the model. The model θ-sections show a relatively well mixed layer over the EEP extending to around 900 mb, while the reanalysis θ-fields suggest strong mixing to around 800 mb. This point is explored in more detail in Part II of this study.

Overall, despite clear differences with the re-analysis, the cross-sections in Figures 7 and 8 do not suggest major deficiencies in the model's equatorial dynamics. The model θ-sections clearly suggest weaker boundary layer mixing than the re-analysis. However, However, it is also possible that NCEP re-analysis θ is somewhat deficient in this data poor region. Aircraft profiles measured over the EEP during September [Paluch et al., 1999] exhibited very shallow (500-1000 m) well-mixed marine boundary layers capped by a strong inversion and high stratification above, similar to the profiles implied by our model's θ distribution. Yin and Albrecht [1999] find evidence for a double inversion structure over the EEP cold-tongue, with a shallow (500-700m) well-mixed "transition layer" capped by an inversion, and a second, weakly-stratified region above this capped by the "trade inversion" at around 800 mb. Neither our model nor the re-analysis appear to reproduce such a structure.

3.2 Oceanic Wind Stresses

Annual Mean and Seasonal Cycle. Figure 9 shows the time-mean zonal and

meridional wind stress along the equatorial Pacific from the model and from SSMI and COADS observations. Agreement between the model and observations is generally good. Extremal values of easterly stress occur between 150W and 140W and have values around -0.06 N m^{-2}. The simulation of the mean zonal wind stress is clearly improved over what was shown in Figure 1 for the earlier version of the GCM. The simulation of the meridional stress is also acceptable, although in the case of meridional stress there is a large disagreement between COADS and SSMI observations in the EEP. The model's meridional stress is in excellent agreement with 1988-1996 SSMI mean, but 0.01 to 0.015 N m^{-2} below the COADS mean.

The model's 20-year mean seasonal cycle of zonal wind stress along the Equator is shown in Figure 10. Although the general pattern of seasonal wind stress variation in the model (Fig. 10a) is well simulated, the amplitude of the cycle is somewhat high compared with that in the COADS and SSMI climatologies (Figs. 10b and 10c). A particularly striking error in the model's seasonal cycle is the strong easterly anomaly during August-October between 160W and 120W. Although not as pronounced, a corresponding westerly error is present in the same longitude band during Feb.-May. Both of these of errors appear to be manifestations of a spurious standing oscillation in the model's zonal stress along the Equator. Part II will explore possible causes for this defect. Positive aspects of the simulation include the general westward propagating character of the stress anomalies in the EEP, the seasonal phasing of minima and maxima in the EEP, and the position of westerly maximum in March-April. The strong semi-annual component present in the earlier version of our AGCM (Figure 2) has been largely eliminated. Figure 10d shows the 20-year mean seasonal cycle of equatorial SST from a free-running coupled GCM experiment using NSIPP-1 as the atmospheric component. Comparison with coupled results using the earlier AGCM (Figure 2) show that the simulated seasonal cycle of SST has in fact improved substantially.

The quality of the simulated annual cycle of zonal wind stress in NSIPP-1 is

13

comparable to that in other models analyzed by Saji and Goswami [1997] for the AMIP project. The peak-to-peak (March-September) amplitude of 0.04 N m^{-2} near 140W is well within the ensemble spread for the AMIP-project models [Fig. 10, Saji and Goswami, 1997]. Although the attribution of propagating character to wind-stress anomalies is somewhat subjective, NSIPP-1 appears to be in the category of models that exhibit propagation (or westward expansion) of anomalies in both the the EEP and equatorial Atlantic, as is in fact observed (Atlantic wind-stresses are not shown here). Our model's excessively strong annual oscillation between 160W and 120W is also clearly present in several of the AMIP-project models.

Figure 11 shows 20-season means (DJF, MAM, JJA and SON) of zonal wind stress across the equatorial pacific for 1979-1999 from the model and from COADS. The simulated wind stress is in excellent agreement with the long term climatological wind stresses obtained from the COADS data set (Fig. 11b,d,f,h), as well as those from the SSMI instrument and the ECMWF re-analysis (not shown). Close inspection reveals the excessive seasonal cycle in the equatorial Pacific between 160W and 120W, with excessive easterly stress during JJA and SON. Other notable biases include excessive westerly stress off the coast of southern Mexico and Central America during JJA and SON. This is almost certainly related to strong low-level convergence induced by or associated with the strong wet bias in the same location (Fig. 5).

Figure 12 shows 20-season averages of meridional wind stress. The agreement with COADS is generally good, although the equatorial meridional stress in the model tends to lower (less southerly) than in the COADS observation. This is especially true during DJF and SON, where the COADS meridional stress in the EEP is close to or above 0.04 N m^{-2}, while the model is closer to 0.02 N m^{-2}. Figure 13 shows seasonal means of wind-stress curl, which is an important control on the amount oceanic upwelling [Gill, 1982]. There is good agreement with the COADS data. The model accurately reproduces the forcing responsible for mid-latitude oceanic gyres in both the Pacific and

14

Atlantic. Equatorial values are weak in both model and observations. However, the gross seasonal variation of wind stress curl in the EEP is reproduced, with large values occurring during JJA and SON.

Interannual Variability. Figure 14 shows a Hovmoeller diagram of interannual zonal wind stress anomalies, along the equatorial Pacific, from 1988 to 1996, from the model and from SSMI. The figure confirms that the model has captured the overall variation of wind stress during this period. The La Niña related westward expansion of strong easterly stresses during 1988 is captured, as is the retreat of strong stresses during the warm early 1990's. Stress anomalies during the La Niña event of 1988-89 are somewhat weaker in the SSMI data than those simulated by the model, but the anomalies during the weaker 1995-96 cold event are similar in both. Figure 15 shows a plot of model and SSMI zonal wind stresses averaged in the box [160E,150W,5S,5N] versus Reynolds SST averaged in the box [150W,90W,5S,5N] (NINO3) for the period January 1988 to June 1996. A 13-month boxcar filter was applied to all time-series before plotting, so that seasonal cycles in SST and wind stress are not included. The figure shows that, overall, the relationship between SST-anomaly and zonal wind stress is nearly linear. The slope of the SST/τ_x relationship is around 2 N m^{-2} K^{-1} for both model and SSMI, although the SSMI relationship (filled circles) appears to be somewhat steeper than the model's, indicating a slightly reduced sensitivity to SST gradients in the model. A large departure from this nearly linear relationship occurs for the SSMI stresses during the 1988-89 La Niña event. The reasons for this are not clear.

3.3 Divergent Circulation

The divergent circulation is the most direct response of the atmosphere to heating. Trenberth et al. [2000] analyzed the divergent circulation in NCEP and ECMWF reanalyses. Their analysis revealed the existence of localized, shallow overturning circulations, which exist in addition to the better known Hadley and Walker circulations.

In the present analysis we first calculate the horizontal divergence, $\mathcal{D} = -\partial_p \omega$, from the time-mean model and re-analysis ω fields on the standard pressure levels given in Table 1. We determine $\mathcal{D}$ at half-levels using fist-order finite-differences. We then invert $\nabla^2 \chi = \mathcal{D}$ to obtain the velocity potential and determine the horizontal divergent wind $\mathbf{u}_\chi = \nabla \chi$. Figure 16 shows the 20-season mean 225 mb velocity potential χ for JAS from the model and from the NCEP re-analysis. Generally, speaking the comparison is very good. The simulated χ field shows a somewhat higher subtropical "ridge" in the northern hemisphere (Eq.-30N) between 150W and 90W. As will be shown below, this region in the model is characterized by excessively strong mid-tropospheric descent.

We now examine average cross-sections of the divergent flow in the boxed regions shown in Figure 16. Figures 17-20 show 20-season mean, divergent flow fields for JFM and JAS from the model and from the NCEP re-analyses. This grouping of months is chosen since it corresponds more closely with the seasonal phasing of minima and maxima in zonal-wind stress along the EEP. Vectors of (u_χ, ω) in the longitude-pressure plane are shown for JFM (Figure 17) and JAS (Figure 18). Vectors of (v_χ, ω) in the latitude-pressure are also shown for JFM (Figure 19) and JAS (Figure 20).

Figures 17 and 18 show model and NCEP re-analysis estimates of the meridionally-averaged, zonally-aligned divergent circulation over the Pacific (Walker Circulation) in three latitude bands; southern tropical, 18S-6S; equatorial, 6S-6N; and northern tropical, 6N-18N. Zonal overturning cells for JFM in the 6S-6N band (Figures 17c,d) and 18S-6S band (Figures 17e,f) generally agree well. Strong upward motion is present in the western Pacific, 100E-160W, and to a lesser degree over South America east of 100W. These regions of ascending motion are forced by moist heating in the SPCZ and ITCZ in the western Pacific, and in summertime precipitation over Amazonia. Ascent over Amazonia appears somewhat less organized in the model. Strong descent is evident in the southern band betwen 120W and 90W. In the equatorial band only weak descent is evident during JFM in both model and re-analyses. The 6N-18N band (Figures 17a,b)

16

exhibits the worst agreement between model and re-analysis. Strong ascent is evident in the model near 110W, which is entirely absent from the re-analysis circulation. This ascent appears to be related to the strong wet bias located near the coast of Mexico during northern winter (Fig. 5a,b). Less easily understood is strong descent in the model located from 150E-180, which does not appear in the re-analysis. This is possibly connected to the model's somewhat excessive precipitation north of the Equator in the warm pool region during northern winter.

During JAS (Figure 18), the center of the Walker circulation moves northward in both model and re-analysis. Intense upward motion is now present in the 6N-18N latitude band (Figures 18a,b) at both western and eastern ends of the Pacific. The model circulation (Figure 18a) exhibits a remarkable downward "chute" of strong descent centered around 130W, which is not present in the re-analysis (Figure 18b). The origins of this descent are not clear, however, they may lie in the alignment of intense precipitation zones in the eastern Pacific, which are more meridionally-aligned in the model than in observations. In the equatorial band (Figures 18c,d) descent over the central and eastern Pacific shows up in the re-analysis as well, although it is less intense and centered at higher altitude than in the model. Further south 18S-6S (Figures 18e,f) descent becomes more widespread, while upward motion becomes weaker and more spatially restricted. The agreement between model and re-analysis for this band is fairly good.

Meridionally-aligned divergent cells (Hadley Circulation) are shown in Figure 19 (for JFM) and Figure 20 (JAS) for three longitude bands; over the Pacific warm pool region, 110E-150E; over the eastern Pacific, 140W-100W; and over South America/Amazonia and the Caribbean, 90W-50W. The overall structure of the deep Hadley circulation is clear over the Pacific warm pool (Figures 19a,b and 20a,b). Both model and re-analysis show a strong core of upward motion, which moves from 5S-10S in JFM (Figures 19a,b) to 10N-15N during JAS (Figures 20a,b). During JFM the agreement between model

and re-analysis in this band is good everywhere. In JAS, the descending flow in the model's southern mid to lower troposphere (1000mb-500mb, 35S-10S, Figure 20a) has a distinct southerly component, which is not the case for the re-analysis.

Moving east to the eastern Pacific band, 140W-100W (Figures 19c,d and 20c,d), there is again agreement in the broad features of divergent circulation, but numerous disagreements in the details of the flow exist. During JFM (Figures 19c,d) both model and re-analysis exhibit a complex superposition of shallow and deep overturning circulations near the Equator. This is particularly clear between 5N and 20N where a shallow cell is clearly present from the surface to around 700 mb. Above this, the model exhibits strong ascent which is not present in the re-analysis. During JAS, the simulated divergent circulation (Figure 20c) again shows evidence of the curious descending "chute" between 5N and 15N, which was noted in Figure 18a. This chute is evidently part of a tortuous stream of descending air originating at around 200 mb near 10N. This stream initially moves southward, then briefly turns north around 300 mb, before turning south again between 500 and 400 mb, and joining a northward moving stream of descending air over the Equator at around 600 mb. The re-analysis circulation for JAS in the same band (Figure 20d) shows a weak but better organized deep cell with weak upward motion between 6N and 18N and descent over the Equator.

In the easternmost band over South America and the Caribbean, 90W-50W, (Figures 19e,f and 20e,f) the overall position of the descending and ascending branches of the circulation are in agreement, but significant differences in the broad features of the flow do exist. During JFM the model's local Hadley circulation (Figure 19e) exhibits a strong southward tilt in the ascending branch (15S-Eq.), particularly between 800 mb and 500 mb. A much weaker southward tilt in the same altitude range is also present in the ascending branch of the re-analysis circulation (Figure 19f). During JAS the ascending branch in both the model and the re-analysis (5N-15N, Figures 20e,f) is tilted northward, although much more so in the model circulation. The origin of the

pronounced tilting in this longitude band is not clear.

A notable similarity between the model and re-analysed divergent flow is the existence of numerous secondary shallow cells, both meridional and zonal, in addition to the well-known, troposphere-deep Hadley and Walker circulations. A particularly clear example of such a cell is the one seen over the eastern Pacific (Figs. 19c and 19d), from the surface to around 600 mb, between 5N and 20N. Trenberth et al. [2000] first identified such secondary circulation features in the NCEP and ECMWF reanalyses. They conducted an EOF analysis, which showed that a large fraction of the seasonal variability in the divergent circulation is accounted for by two modes, roughly speaking: a deep mode extending from the surface to around 100 mb with a node at around 550 mb; and a shallow mode, extending from the surface to around 550 mb with a node around 850 mb [Trenberth at al. 2000, Figure 1].

Based on Trenberth et al.'s analysis we define a deep mode $T_d(p)$ and a shallow mode $T_s(p)$ according to;

$$
T_{d,s}(p) = \begin{cases} 0 & p < p_t \\ \frac{\mathcal{B}}{p_n - p_t} & p_n > p \geq p_t \\ \frac{-\mathcal{B}}{p_{sfc} - p_n} & p_{sfc} \geq p \geq p_n \end{cases} \tag{1}
$$

where for T_d we use $p_t = 100$ mb and $p_n = 550$ mb, and for T_s we use $p_t = 550$ mb and $p_n = 850$ mb. Both modes have $p_{sfc} = 1000$ mb. The normalization constant $\mathcal{B}$ is chosen so that $p_{sfc}^{-1} \int_0^{p_{sfc}} T_{d,s}(p) T_{d,s}(p)\ dp = 1$. We can then project any quantity $X(\lambda, \phi, p, t)$ onto T_d and T_s;

$$
\widehat{X}^{d,s} \equiv \frac{1}{p_{sfc}} \int_0^{p_{sfc}} T_{d,s}\ X\ dp \tag{2}
$$

to obtain time-varying, horizontal maps of its deep and shallow components. Note that $\widehat{T_d}^s = \widehat{T_s}^d = 0$. Also, note that the modes in (1) are defined such that the sign of the fluctuations is positive in the upper half, so that, for example, positive $\widehat{\mathcal{D}}^d$ implies divergence in the upper troposphere troposphere and convergence at low levels.

19

Figure 21 shows the 20-season means of $\widehat{u_\chi}^{d,s}$, $\widehat{v_\chi}^{d,s}$, and $\widehat{\mathcal{D}}^{d,s}$ for JAS and JFM from the model and from the NCEP re-analysis. First of all, we note that the structure of the deep and shallow circulations derived from (1,2) for the NCEP re-analyses are indeed similar to those derived by Trenberth et al., (c.f. Figs. 2 and 3 of that study) using a more rigorous EOF analysis. Next we note that, the overall horizontal structure of the model's deep and shallow circulations is similar to that found in the NCEP re-analyses. Pronounced shallow overturing cells are evident (Figures 21c,d,g,h) including a cell with strong, shallow divergence centered over Australia during JFM (Figures 21c and 21d). Another shallow cell straddles the Equator in the east and central Pacific (120W-90W). This cell is the one previously identified in the 140W-100W meridional sections for JFM (Figs. 19c,d), with rising motion immediately north of the Equator. During JAS, this Pacific shallow cell (Figs. 20g and 20h) shifts north, and the main descending branch, indicated by converging flow aloft, switches from the northern to the southern flank of the rising motion. This switch is particularly pronounced for the model. A notable difference between the model and re-analysis in both seasons, is that the model shallow circulation appears better organized as well as more concentrated. The model's shallow circulation exhibits a continuous strip of strong upper-branch divergence $\widehat{\mathcal{D}}^s$ across the Pacific. Interestingly, neither model nor re-analysis shallow circulations closely follow the precipitation distribution, while the deep circulations do.

By contrast, the upper-branch divergence in the deep circulation (Figures 21a,b,e,f) roughly resembles the corresponding precipitation distribution in all seasons. There is some suggestion of more ITCZ splitting in the central Pacific in the re-analysis $\widehat{\mathcal{D}}^d$ for JAS (Figure 20f) than in the corresponding CMAP precipitation estimate (Figure 5d). This probably reflects a disagreement between the re-analyzed precipitation field (not shown) and the CMAP estimate. Nevertheless, the connection between upper tropospheric divergent flow and precipitation is clear in both the model and in the re-analysis. In the deep divergent circulation for JFM from both the model and the

re-analysis (Figs 20a and 20b), strong northward cross-equatorial flow is present over much of the western Pacific. This flow appears to emanate from the SPCZ. However, in the model, the deep divergent flow associated with both the SPCZ and ITCZ appears more concentrated. The upper-branch mass source immediately north of the Equator in the western Pacific (150E,2N) is stronger in the model relative to rest of the deep circulation than in the re-analysis. The model deep circulation in JFM also possesses a strong, apparently spurious mass source west of Mexico near (100W,15N), which is connected to the northern winter precipitation bias at the same location (c.f. Figs. 5a,b). This leads to the the ascent evident between 120W and 100W in in the 6N-18N latitude-pressure section through the divergent flow (Figure 16e). The strong descent evident between 150E and 160W in the same longitude-pressure section appears to be related to a zone of strong upper-branch convergence forced by the mass-sources over the western Pacific SPCZ/ITCZ and possibly the eastern Pacific.

During JAS, the clearest difference between model and re-analysis circulations is the pronounced separation in the model's ITCZ-related upper-level mass source. The model shows strong upper-level divergence over the eastern Pacific and Mexico, and also over the warm pool region (120E-150E). These mass-sources, in particular the one over Mexico, appear more meridionally aligned than the corresponding upper-level mass-sources in the re-analysis. This meridional alignment appears to contribute to upper-level convergence, and thus forced descent, over much of the eastern Pacific (150W-110W) in the model. This is also evidently the origin of the odd "chute" of descending air in Figure 17e between 140W and 120W, which is seen in Fig. 20e to be a region of descent connecting subtropical highs in eastern Pacific north and south of the ITCZ.

21

5. Summary and Discussion

This is the first part of a two part study. Here (Part I) we seek to document the model's basic performance in a 20-year (1979-1999), forced-SST experiment. Our principal areas of concern are the model's equatorial dynamics and the model's simulation of wind stress over eastern equatorial Pacific (EEP), a key region in coupled ENSO dynamics. In Part II of this study, we conduct a detailed analysis of the model's momentum budget in the equatorial region. We use this analysis to suggest links between specific processes such as boundary layer mixing, or precipitation, and aspects of surface wind stress simulation over the EEP.

NSIPP-1's simulation of extratropical, boreal-winter planetary waves (Fig. 3) was found to be excellent compared with that found in other AGCMs [e.g., Gates et al., 1999]. We also found a good simulation of ENSO-related planetary wave variability (Fig. 4), which is critical to obtaining believable dynamical seasonal predictions from the model [Shukla et al. 2000]. The model's simulation of mean precipitation (Figs. 4) was also generally good, as was the simulated ENSO-response in tropical precipitation (Fig. 5). Nevertheless, numerous bias are evident in the model's precipitation, which may be related to biases in wind-stress. In particular, we observe that the model's Pacific ITCZ during northern summer tends to "split", leaving the east central Pacific (150W-120W) relatively dry, while the extreme eastern Pacific is wet.

The model's simulation of annual-mean, as well as interannually-varying, wind stresses appears to be quite good. Equatorial annual-mean profiles of both zonal and meridional stress are in excellent agreement with observations (Fig. 9). Interannual variability in zonal wind stress is also generally well simulated when compared with SSMI observations (Fig. 14). The major problems in the model's wind stress simulation appear in the seasonal cycle (Fig. 10). While some aspects of the observed seasonal cycle in wind stress are captured, including the general westward propagating character of anomalies in the EEP, signifcant biases are evident. Overall, the model's seasonal cycle

22

is too intense by a factor of around 1.2-1.5. Furthermore, significant departures from the observed pattern of seasonal variation do occur. These are most evident in broad (40°) longitude band centered near 140W. Here a spurious, standing annual oscillation in wind stress anomaly appears to combine with the propagating anomaly pattern seen in the observations, to give a pronounced easterly error during August-October. In Part II many of these biases are traced to excessive "deep" forcing of wind stress in the model.

Finally, we examined our model's divergent circulation in the Equatorial region. This is of interest both because the divergent circulation is an indicator of the model's heating field that can be directly compared with re-analysis fields, and because the divergent circulation is an intuitively clear connection between atmospheric heating, particularly that associated with convection, and possible long-distance effects of such heating. The overall pattern of the divergent circulation in the model is similar to that found in NCEP re-analyses. However, significant differences do exist. A possibly critical difference between model and re-analysis is the presence of strong mass convergence (forced descent) over the central and eastern equatorial Pacific in the model. This convergence originates in both shallow and deep divergent circulations, and varies seasonally, with the strongest convergence occurring during boreal late summer and fall (JAS+October). The seasonal phasing as well as the location (140W-100W) of this forced descent suggests a connection with the errors in the model's simulated seasonal cycle of zonal wind stress. In Part II we demonstrate that the flaws in the model's wind stress seasonal cycle can in fact be traced to free-tropospheric processes rather than boundary layer dynamics. This lends support to a possible connection between model errors in wind stress and in the divergent circulation. This also supports a connection between precipitation biases and wind stress errors as speculated by Saji and Goswami [1997].

References

Arakawa, A. and M.J. Schubert, Interaction of a cumulus cloud ensemble with the large scale environment, Part I, *J. Atmos. Sci., 31,* 671-701, 1974.

Arakawa, A. and M.J. Suarez, Vertical differencing of the primitive equations in sigma coordinates. *Mon. Weather Rev., 111,* 34-45, 1983.

Bacmeister, J. T., P. J. Pegion, S. D. Schubert, and M. J. Suarez, Atlas of seasonal means simulated by the NSIPP-1 atmospheric GCM, *NASA Technical Memorandum 104606, 17,* 194pp, 2000.

Bacmeister, J. T., and M. J. Suarez, Wind-stress simulations and equatorial dynamics in an AGCM Part II: Equatorial momentum budget and its relation to oceanic wind stress, *J. Atmos. Sci., (submitted* 2001).

Chou, M.-D. and M. J. Suarez, 1994: An efficient thermal infrared radiation parameterization for use in general circulation models. NASA Technical Memorandum, 104606, **10**, 84pp.

Chou, M.-D. and M. J. Suarez, 1999: A solar radiation parameterization for atmospheric studies, NASA Technical Memorandum, 104606, **11**, 40pp.

Da Silva, A., C.C. Young, and S. Levitus, Atlas of Surface Marine Data 1994 Vol. I: Algorithms and Procedures. NOAA Atlas NESDIS 6, U.S. Dept. Of Commerce, Washington, D.C., 83 pp.,1994.

Daubechies, I., Ten Lectures on Wavelets. Society for Industrial and Appl. Math., 1992.

Gates, W. L., J. S. Boyle, C. Covey, C. G. Dease, C. M. Doutriaux, R. S. Drach, M. Fiorino, P. J. Gleckler, J. J. Hnilo, S. M. Marlais, T. J. Phillips, G. L. Potter, B. D. Santer, K. R. Sperber, K. E. Taylor, and D. N. Williams, An Overview of the Results of the Atmospheric Model Intercomparison Project (AMIP I), *Bull. Am. Met. Soc., 80,* 29-56, 1999.

Gill, A. E., Some simple solutions for heat induced tropical circulations, *Quart. J. Roy. Meteor. Soc., 106,* 447-462, 1980.

Kalnay, E., M. Kanamitsu, R. Kistler, W. Collins, D. Deaven, J. Derber, L. Gandin, S. Sara, G. White, J. Woollen, Y. Zhu, M. Chelliah, W. Ebisuzaki, W. Higgins, J. Janowiak, K. C. Mo, C. Ropelewski, J. Wang, A Leetma, R. Renolds, R Jenne, The NMC/NCAR reanalysis project, *Bull. Am. Met. Soc., 77,* 437-471, 1995.

Lindzen, R. S. and S. Nigam, On the role of sea surface temperature gradients in forcing low level winds and convergence in the tropics, *J. Atmos. Sci., 44,* 2418-2436, 1987.

Louis, J., M. Tiedtke, J. Geleyn, A short history of the PBL parameterization at ECMWF, in *Proceedings, ECMWF Workshop on Planetary Boundary Layer Parameterization, Reading, U. K.,* 59-80, 1982.

Moorthi, S., and M. J. Suarez, Relaxed Arakawa-Schubert: A parameterization of moist convection for general circulation models, *Mon. Weather Rev., 120,* 978-1002, 1992.

Paluch I. R., G. McFarquhar, D. H. Lenschow, et al. Marine boundary layers associated with ocean upwelling over the eastern equatorial Pacific Ocean *J. Geophys. Res., 104,* 30913-30936, 1999.

Pegion, P.J., S.D. Schubert and M.J. Suarez, An Assessment of the Predictability of Northern Winter Seasonal Means with the NSIPP 1 AGCM, NASA Technical Memorandum, 104606, **17**, 150pp, 2000.

Reynolds, R. W., A real-time global sea surface temperature analysis, *J. Climate, 1,* 75-86, 1988.

Saji, N. H., and B. N. Goswami, Intercomparison of the seasonal cycle of tropical surface stress in 17 AMIP atmospheric general circulation models, *Clim. Dyn.,*

13, 561-585, 1997.

Saravanan, R., and J. C. McWilliams, Multiple equilibria, natural variability, and climate transitions in an idealized ocean-atmosphere model, *J. Climate, 8,* 2296-2323, 1995.

Schopf, P. S., and A. Loughe, 1995: A reduced gravity isopycnal ocean model: Hindcasts of El Niño. *Mon. Weather Rev., 123,* 2839-2863

Shukla, J., L. Marx, D. Paolino, D. Straus, J. Anderson, J. Ploshay, D. Baumhefner, J. Tribbia, C. Brankovic, T. Palmer, Y. Chang, S. Schubert, M. Suarez, and E. Kalnay, Dynamical Seasonal Prediction, *Bull. Am. Met. Soc., 81,* 2593-2606, 2000.

Slingo, J. M., The development and verification of a cloud prediction scheme for the ECMWF model, *Quart. J. Roy. Meteor. Soc., 113,* 899-927, 1987.

Suarez, M. J. and L. L. Takacs, Documentation of the Aries/GEOS dynamical core Version 2, *NASA Technical Memorandum 104606, 10,* 56pp, 1995.

Sud, Y. and A. Molod, The roles of dry convection, cloud-radiation feedback processes and the influence of recent improvements in the parameterization of convection in the GLA GCM, *Mon. Weather Rev., 116,* 2366-2387, 1988.

Trenberth, K. E., D. P. Stepaniak and J. M. Caron, The global monsoon as seen through the divergent circulation, *J. Climate, 13,* 3969-3993, 2000.

Wentz F. J., A well-calibrated ocean algorithm for SSM/I, J. Geophys. Res., Vol. 102, 8703-8718, 1997.

Xie, P., and P. Arkin, Global precipitation, a 17-year monthly analysis based on gauge observations, satellite estimates and numerical model outputs, *Bull. Am. Met. Soc., 78,* 2539-2558, 1997.

Yin, B. and B. A. Albrecht, Spatial variability of atmospheric boundary layer structure over the eastern equatorial Pacific, *J. Climate, 13,* 1574-1592, 2000.

Yu, Z., and P. S. Schopf, Vertical Eddy Mixing in the Tropical Upper Ocean: Its Influence on Zonal Currents, Journal of Physical Oceanography: Vol. 27, 1447-1458, 1997.

σ	p (mb)
0.9925	1000
0.9775	
0.9625	
0.9475	
0.9325	
0.9175	925
0.9025	
0.8875	
0.8725	
0.8575	850
0.8375	
0.8125	
0.7875	
0.7625	
0.7250	700
0.6625	
0.5625	600
0.4625	500
0.4000	400
0.3500	
0.3000	300
0.2500	250
0.2125	
0.1875	200
0.1625	
0.1375	150
0.1125	
0.0875	100
0.0625	70
0.0375	50,30
0.0200	20
0.0125	
0.0075	10
0.0025	

Table 1:
First column gives values of the 34 mid-layer σ-levels used in NSIPP-1. Second column gives nearby standard pressure levels used for pressure-level model outputs and NCEP re-analysis fields (in mb).
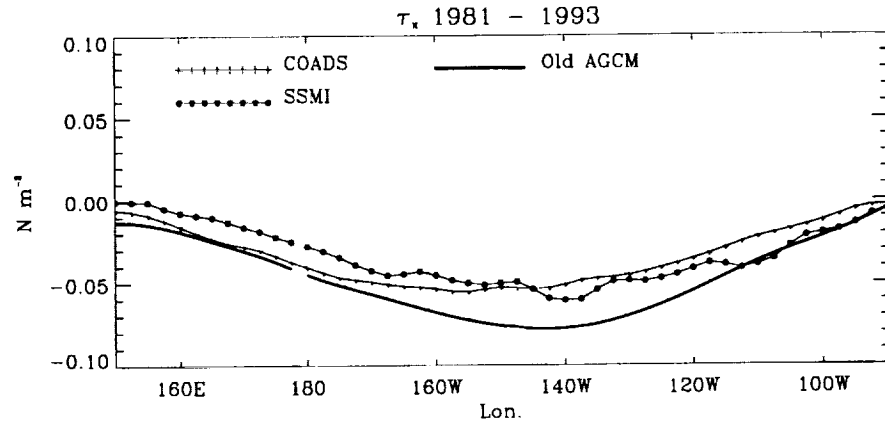
Figure 1: Time-mean zonal equatorial wind stress as a function of longitude. Wind stress is averaged in 3S to 3N band. Solid line shows 1980-1993 annual mean from AMIP-type simulation using an earlier version of the AGCM used in this study. Crosses show 1949-1989 mean from COADS. Filled circles show 1988-1996 SSMI mean.
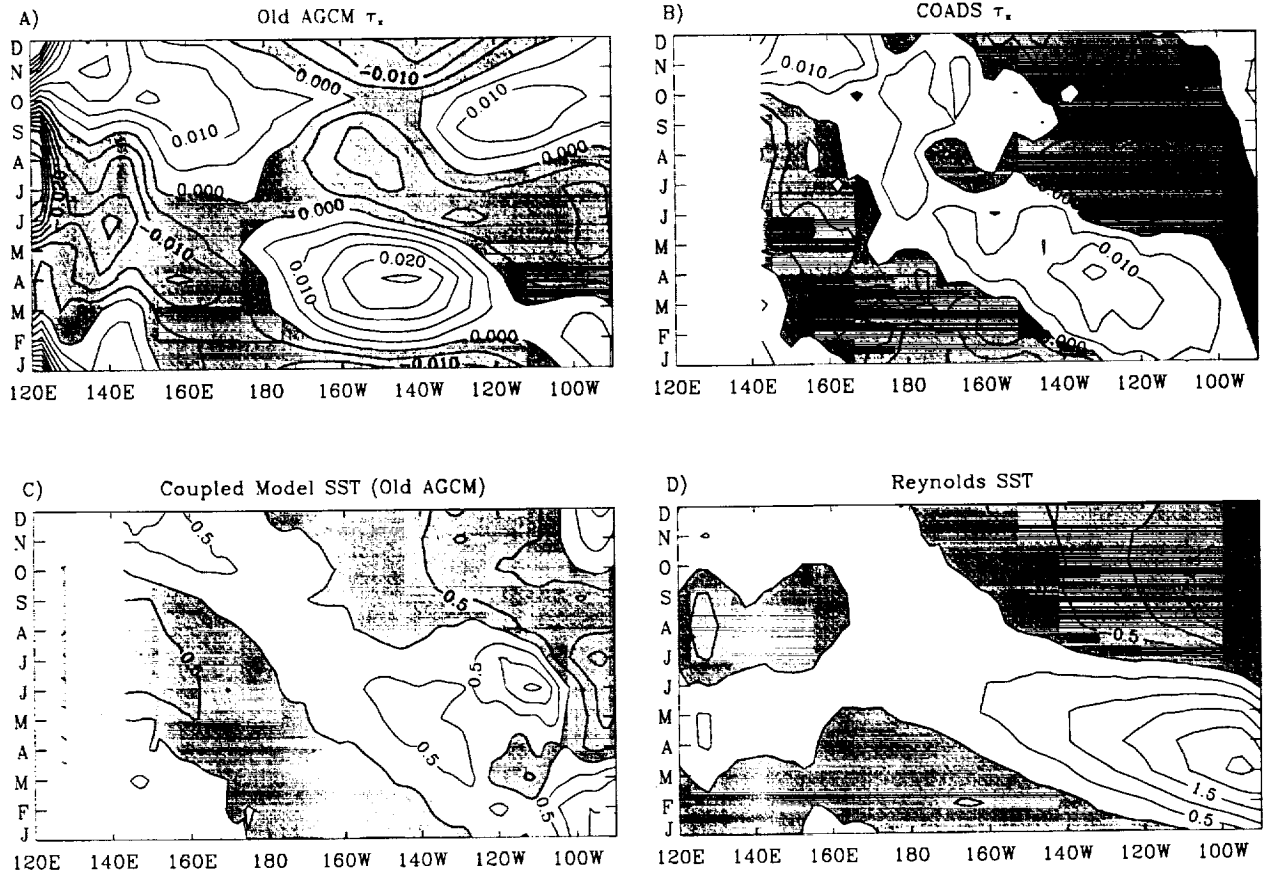
Figure 2: Mean seasonal-cycles of equatorial (3S-3N) wind-stress and SST as a function of longitude and calendar month: a) 1980-1993 mean seasonal cycle of zonal wind-stress from AMIP run using the old AGCM; b) as (a) for 1945-1989 COADS stresses; c) 20-year mean seasonal cycle of SST from free-running CGCM simulation using the old AGCM as the atmospheric component; and d) 1979-1999 mean seasonal cycle of Reynolds SST. Contour interval in (a) and (b) is 0.005 N m^{-2}. Contour interval in (c) and (d) is 0.5 K. Negative anomalies are shaded.
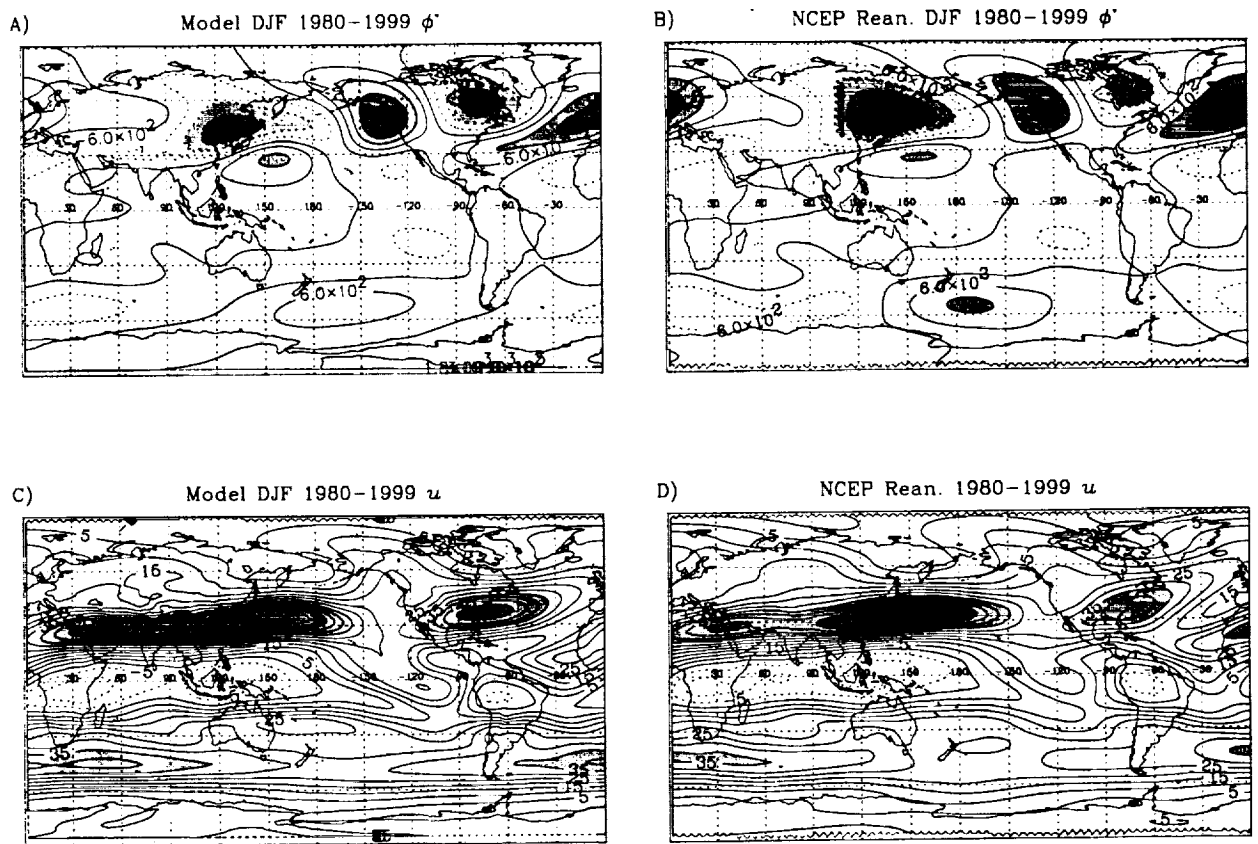
Figure 3: 20 season mean upper air fields for December-January-February (DJF) climate from 1980-1999 AMIP run using NSIPP-1 and NCEP/NCAR re-analyses: a) Geopotential height anomaly (from zonal-mean) ϕ^* from the model, contour interval is 600 geopotential meters, dashed contours indicate negative values, and light and dark shading indicate absloute values above 1200 m and 1800 m respectively; b) as (a) except for re-analysis; c) zonal wind u from the model, contour interval is 5 m s^{-1}, dashed contours indicate negative values, and light and dark shading indicate absloute values above 35 m s^{-1} and 50 m s^{-1} respectively; d) as (c) except for re-analysis.
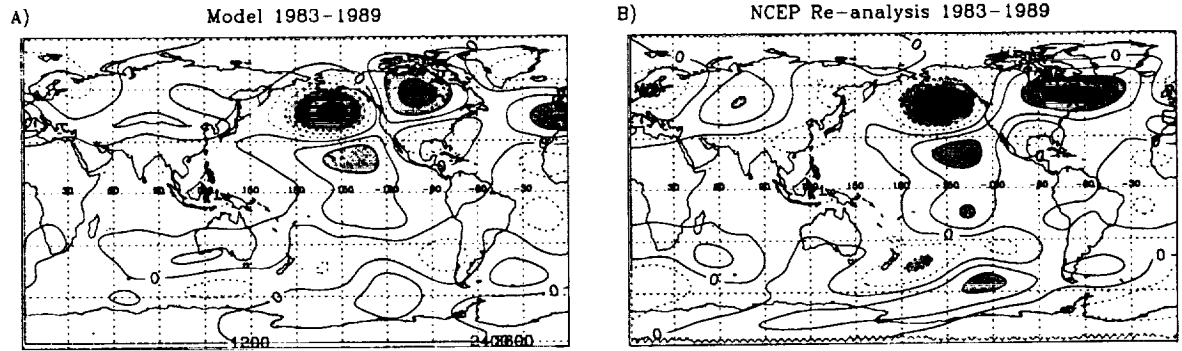
Figure 4: Extratropical ENSO response in for DJF in ϕ^*. Figure shows ϕ^* for DJF 1982-1983 minus ϕ^* for DJF 1988-1989; a) for model, and b) for NCEP/NCAR re-analysis. Contouring is as in Figure 3a and 3b.

A) Model DJF 1980 1999 Precip   B) Xie-Arkin DJF 1980-1998 Precip

C) Model JAS 1980 1999 Precip   D) Xie-Arkin JAS 1980-1999 Precip
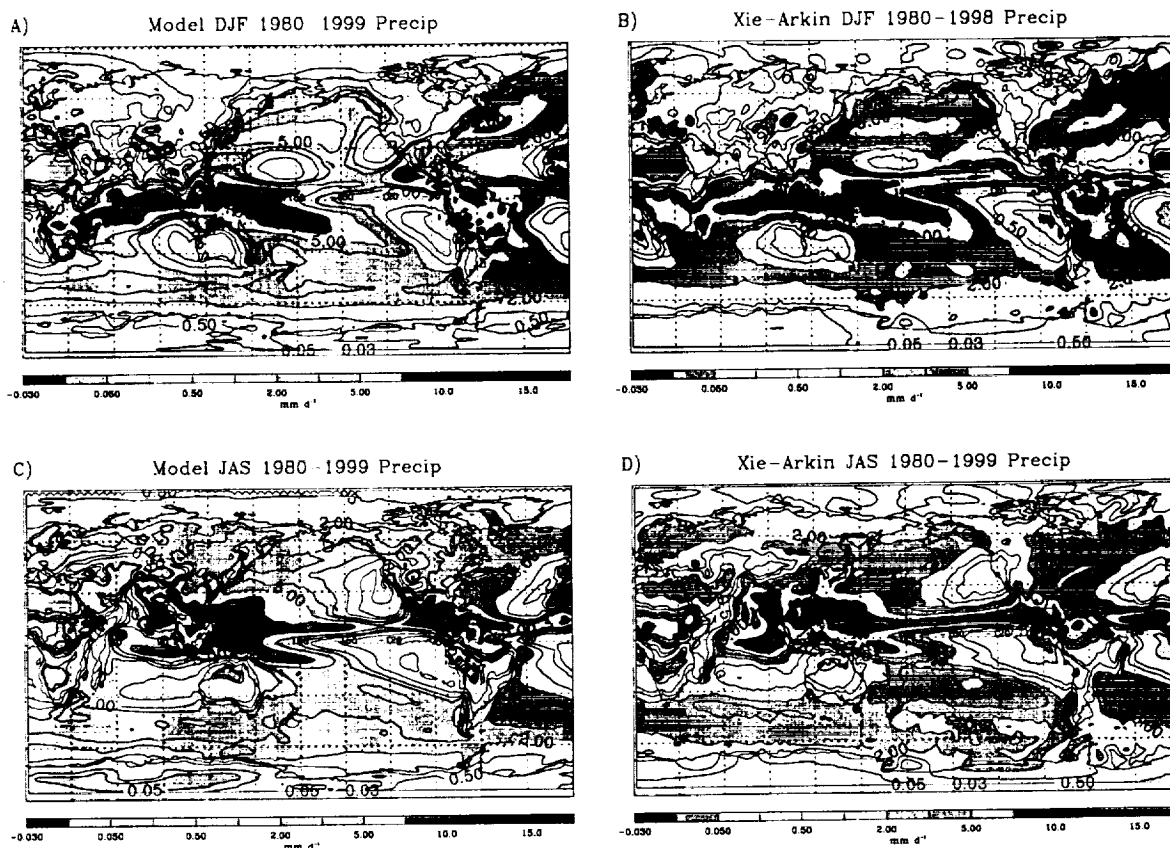
Figure 5: Seasonal averages of precipitation for 1980-1999: a) for DJF in model, contours are drawn for 0.05, 0.1, 0.5, 1.0, 2.0, 3.0, 5.0, 8.0, 10.0, 12.0, 15.0, and 20.0 mm d^{-1}, color table is indicated below each panel; b) as (a) except for Xie-Arkin precipitation data; c) as (a) for JAS in model; d) as (a) except for JAS Xie-Arkin precipitation data.

A) Model DJF 1997/98 Precip. Anomaly B) Xie-Arkin DJF 1997/98 Precip. Anomaly

-20.0-15.0-10.0-8.00-6.00-4.00-3.00-2.00-1.000.00 1.00 2.00 3.00 4.00 6.00 8.00 10.0 15.0 20.0   -20.0-15.0-10.0-8.00-6.00-4.00-3.00-2.00-1.000.00 1.00 2.00 3.00 4.00 6.00 8.00 10.0 15.0 20.0

C) Model JAS 1999 Precip. Anomaly D) Xie-Arkin JAS 1999 Precip. Anomaly

-20.0-15.0-10.0-8.00-6.00-4.00-3.00-2.00-1.000.00 1.00 2.00 3.00 4.00 6.00 8.00 10.0 15.0 20.0   -20.0-15.0-10.0-8.00-6.00-4.00-3.00-2.00-1.000.00 1.00 2.00 3.00 4.00 6.00 8.00 10.0 15.0 20.0

Figure 6: Precipitation fields for El Niño and La Niña extremes: a) model precipitation for DJF 1997/98 (El Niño); b) as (a) except for Xie-Arkin precipitation data; c) model precipitation for JAS 1999 (La Niña); d) as (c) except for Xie-Arkin precipitation data. Contouring and colors are as in Figure 5.
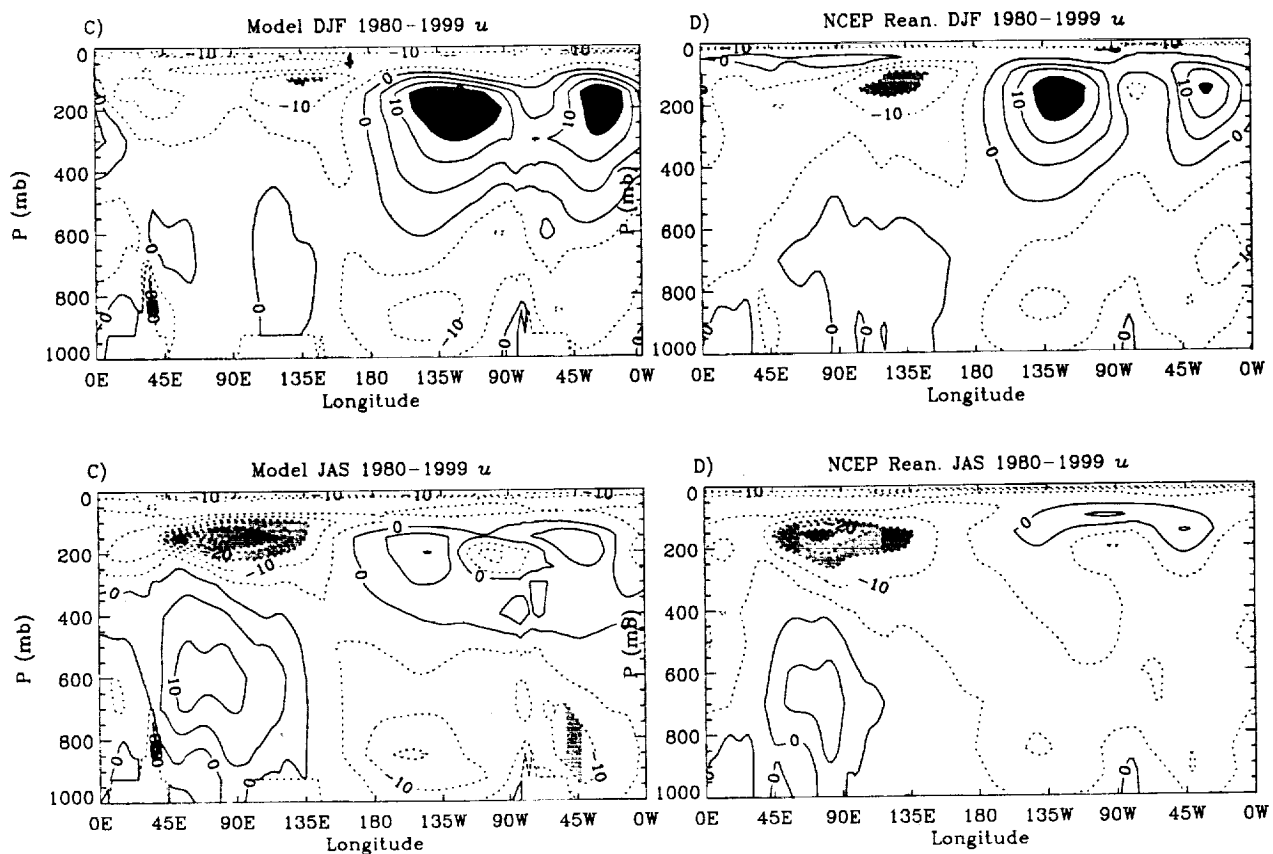
Figure 7: Equatorial zonal wind u as a function of longitude and pressure. 20-season means for 1980-1999, averaged in a band from 3S to 3N are shown: a) model u for DJF, contour interval is 5 m s^{-1}, dashed contours indicate negative values; b) as (a) except for NCEP/NCAR re-analysis; c) as (a) except for model u during JAS; d) as (c) except for except for NCEP/NCAR re-analysis.
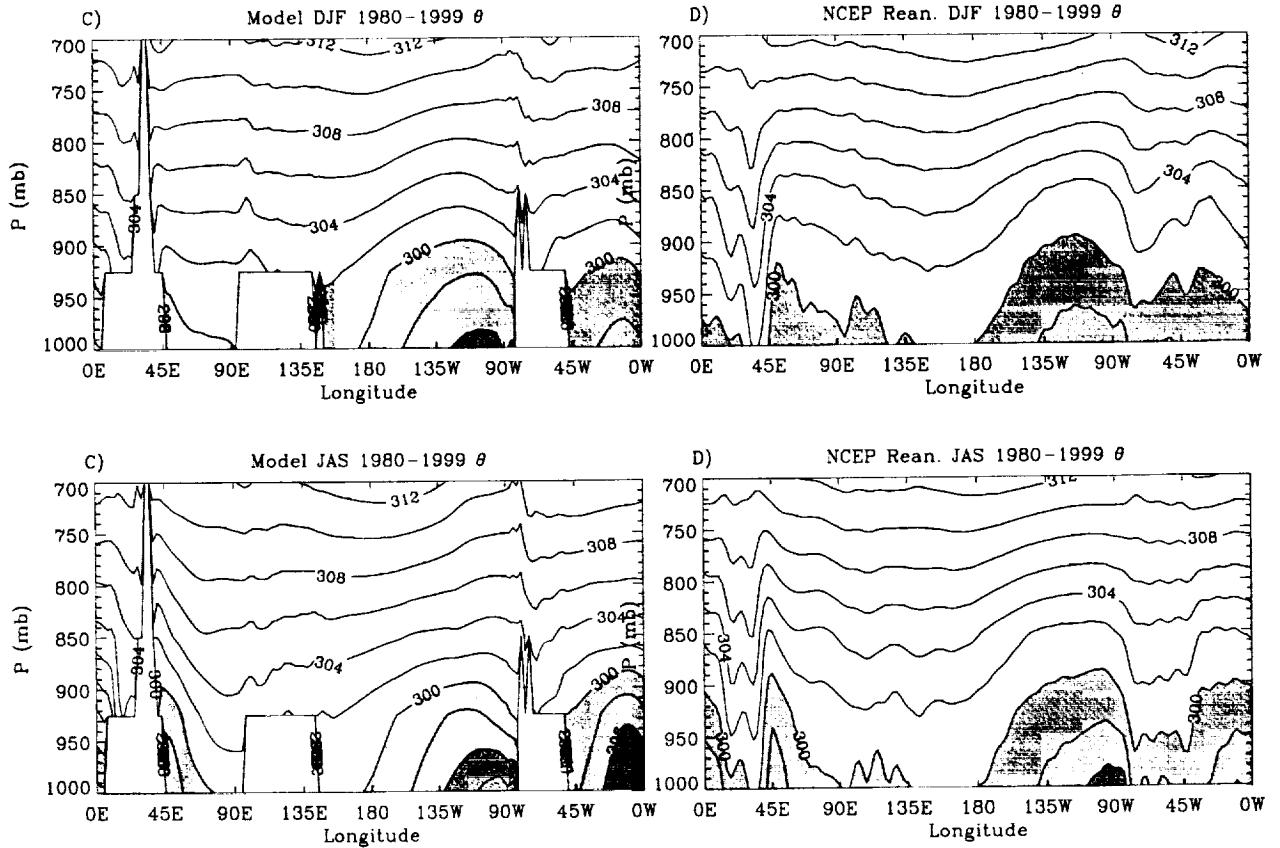
Figure 8: Equatorial potential temperature θ as a function of longitude and pressure. 20-season means for 1980-1999, averaged in a band from 3S to 3N are shown: a) model θ for DJF, contour interval is 2K below 328K and 4K above 328K, light shading indicates values above 332K or below 300K, and darker shading indicates values above 352K or below 296K; b) as (a) except for NCEP/NCAR re-analysis; c) as (a) except for model θ during JAS; d) as (c) except for except for NCEP/NCAR re-analysis.
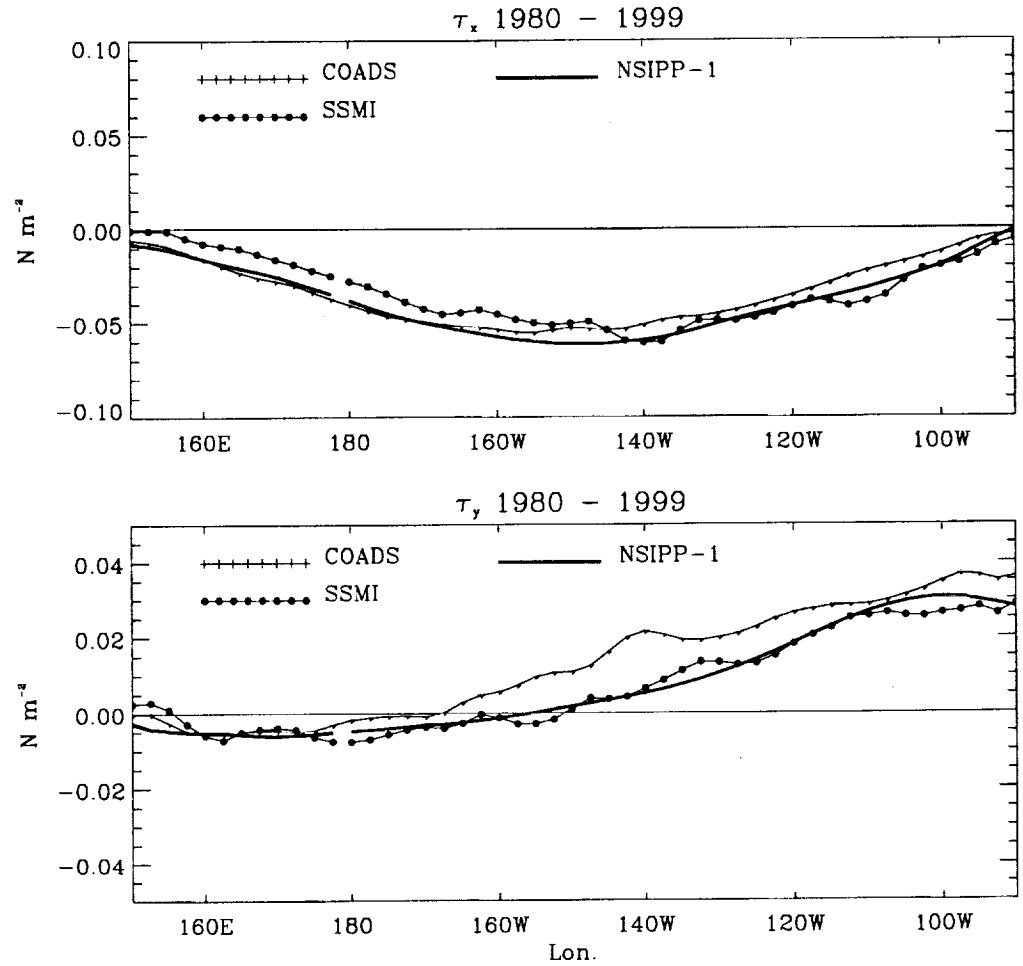
Figure 9: 20-year of zonal and meridional wind stress along the Equator. Averages in a band from 3S to 3N are shown: Upper panel shows zonal wind stress, thick solid line shows model profile, filled circles show SSMI profile, and crosses show COADS; lower panel is as upper panel except for meridional stress.
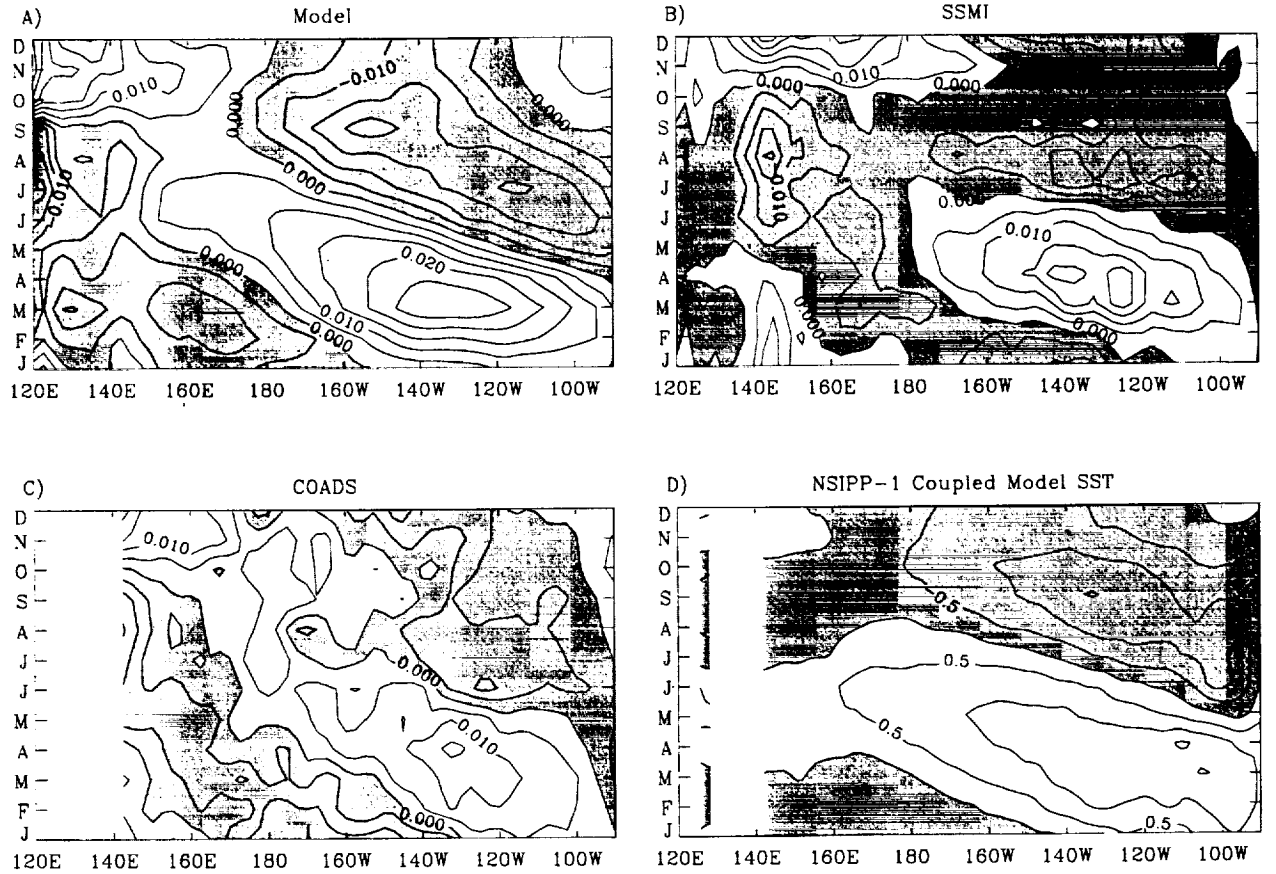
Figure 10: Mean seasonal-cycles of equatorial (3S-3N) wind-stress and SST as a function of longitude and calendar month: a) 1980-1999 mean seasonal cycle of zonal wind-stress from NSIPP-1 AMIP run; b) as (a), for 1988-1996 SSMI zonal-stresses; and c) as (a), for 1945-1989 COADS stresses; d) mean seasonal cycle of SST from free-running coupled GCM experiment using NSIPP-1 as the atmospheric component. Contour interval in (a-c) is 0.005 N m^{-2}. Contour interval in (d) is 0.5 K. Negative anomalies are shaded.
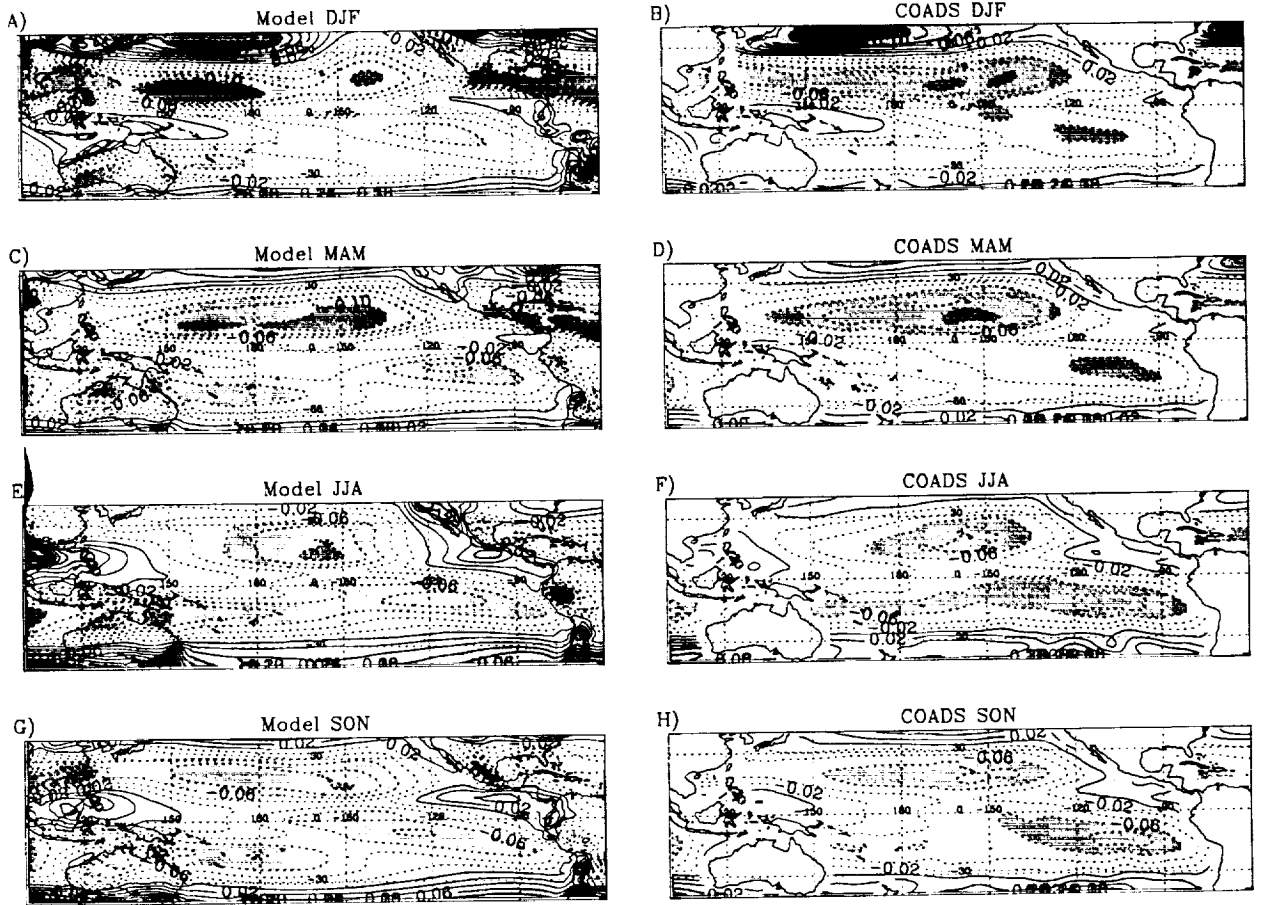
Figure 11: Seasonal means of zonal wind stress from NSIPP-1 and COADS as functions of longitude and latitude: a) model mean for 1980-2000 DJF; b) COADS 1949-19xx DJF; c) model MAM; d) COADS MAM; e) model JJA; f) COADS JJA; g) model SON; h) COADS SON. Contour interval is 0.02 N m^{-2}. Dashed contours indicate negative (easterly) values. Light shading indicates absolute magnitudes above 0.06 N m^{-2}. Darker shading indicates absolute magnitudes above 0.1 N m^{-2}
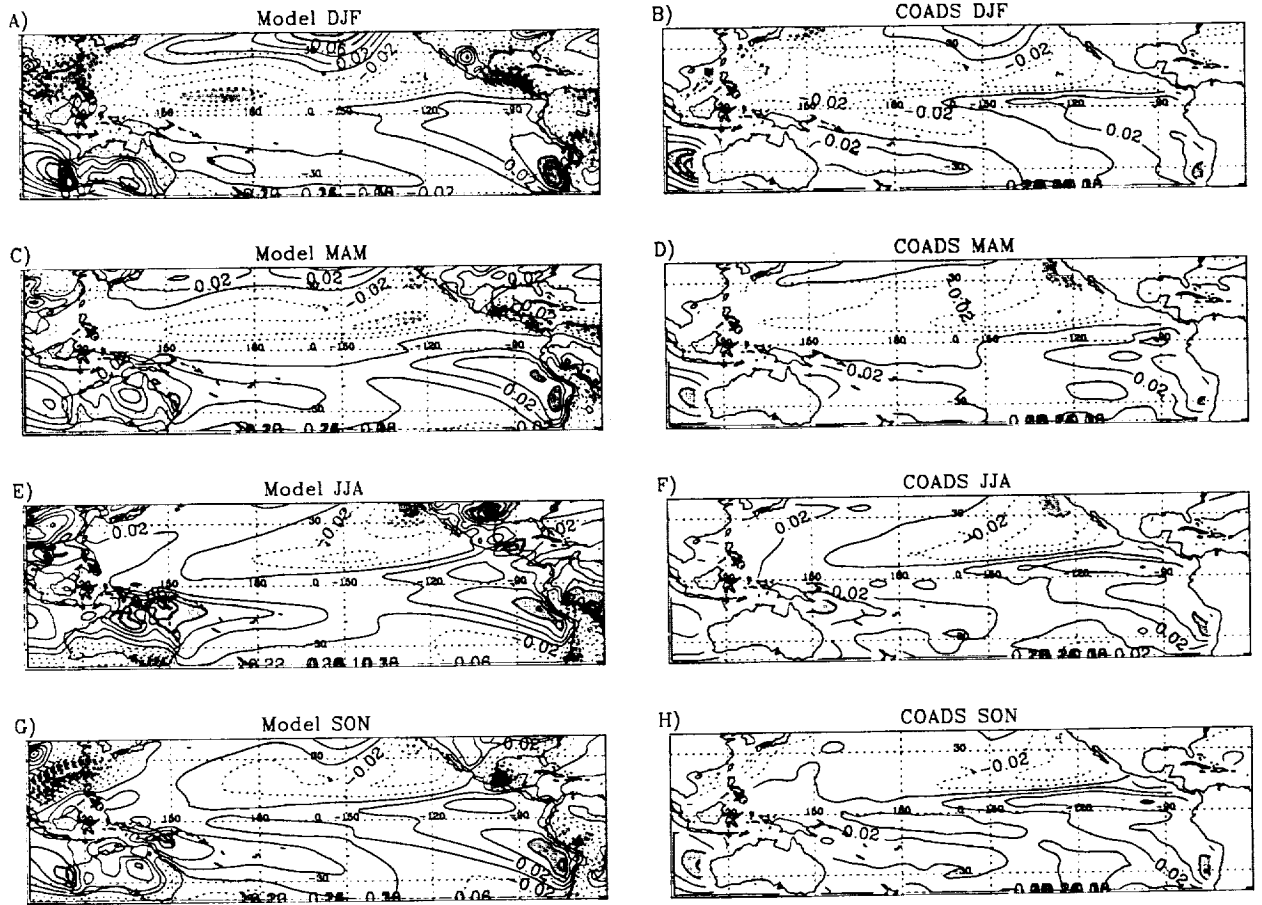
Figure 12: As Figure 11 except for meridional stress. Note negative values indicate southerly stresses.
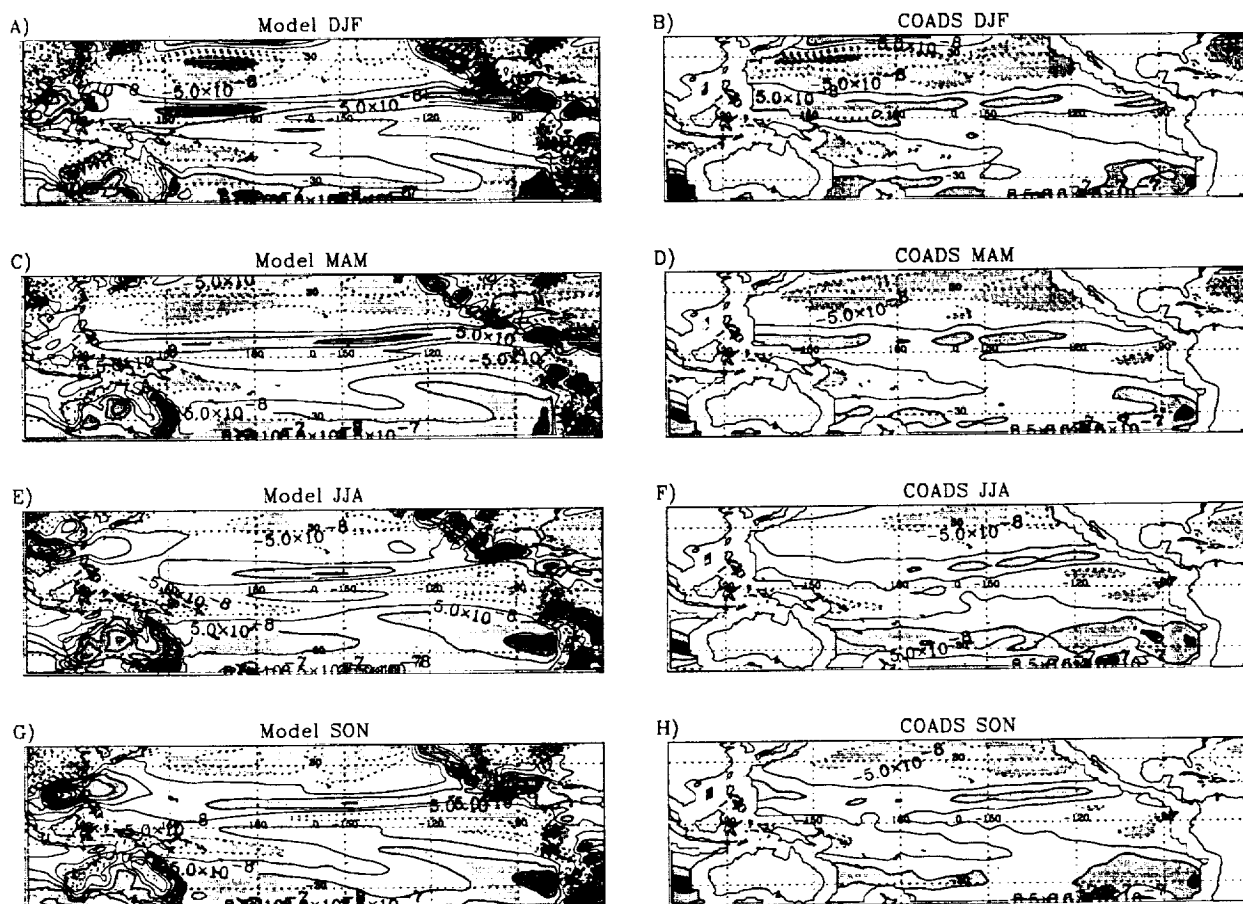
Figure 13: As Figure 11 except for wind stress curl. Note negative values indicate southerly stresses.
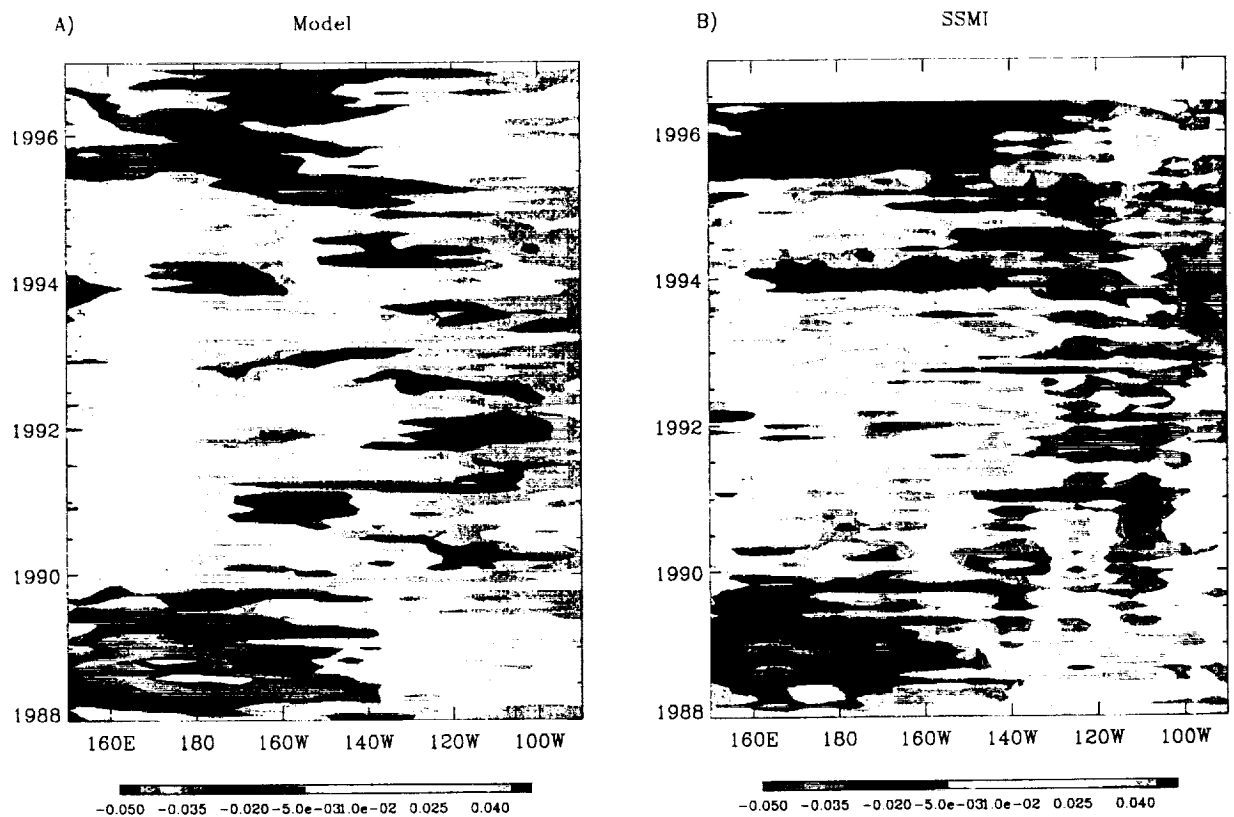
Figure 14: Equatorial (2.5S-2.5N), interannual, zonal wind stress anomalies as a function of longitude and time from 1988 through 1996. Anomalies are calculated from the mean seasonal cycle for the same period. Color bars below each panel indicate range of values in units of N m^{-2}. Yellow-to-red indicates positive or westerly anomalies, i.e., relaxation of the climatological easterly trades. Blue-to-violet indicates negative or easterly anomalies, i.e., strengthening of the trades. Strong easterly anomalies are associated with La Niña events, e.g., 1988-89, while westerly anomalies are associated with El Niño events.
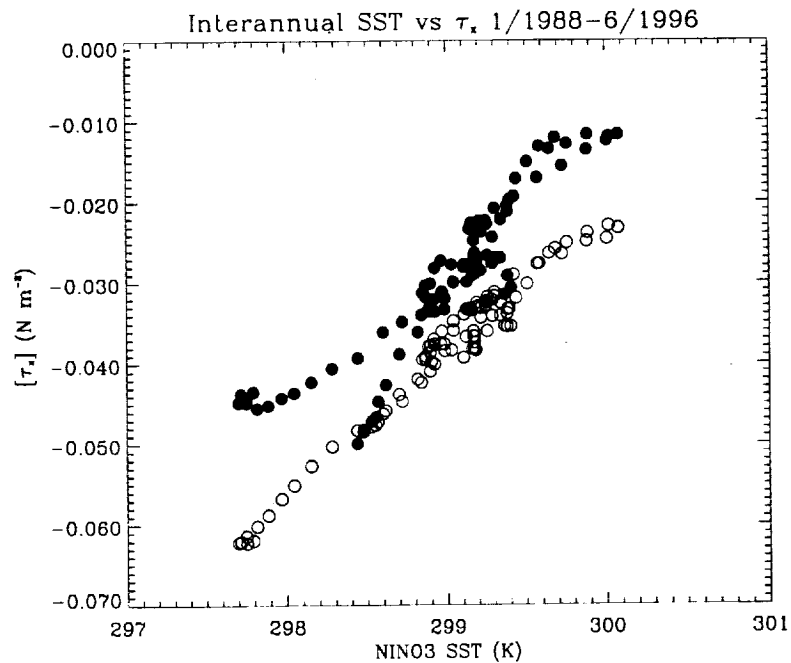
Figure 15: Zonal wind stress vs. sea-surface temperature (SST) for 1988-1996. SSTs have been averaged in the NINO3 region, a box extending from 5S to 5N and from 150W to 90W. Wind stress has been averaged in a box extending from 5S to 5N and from 160E to 150W. The monthly time-series of these averaged stress and SST values were then also time-filtered using 13-month boxcar average to eliminate seasonal variability. Open circles show result from model. Filled circles show result for SSMI wind stresses. Note that in both cases the same Reynolds SST data is used.
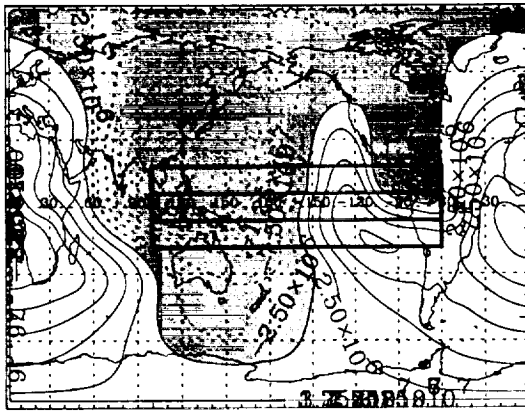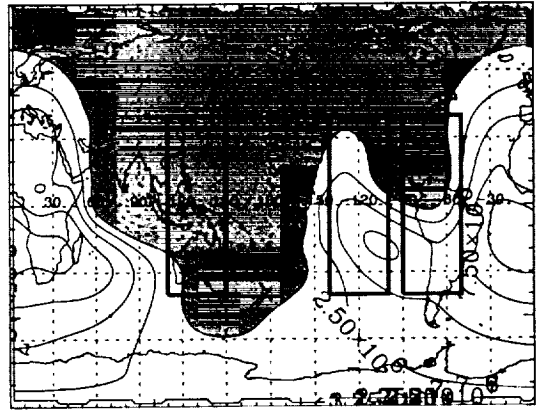
Figure 16: 1980-1999 JAS Seasonal mean of velocity potential χ at 200 mb; a) from the model, b) from NCEP re-analyses. Zonally-aligned boxes in (a) show regions for which latitude-averaged divergent flow is shown as a function of longitude and pressure in Figure 17 and Figure 18. Boxes in (b) show regions for which longitude averaged divergent flow as a function of latitude and pressure is shown in Figure 19 and Figure 20.
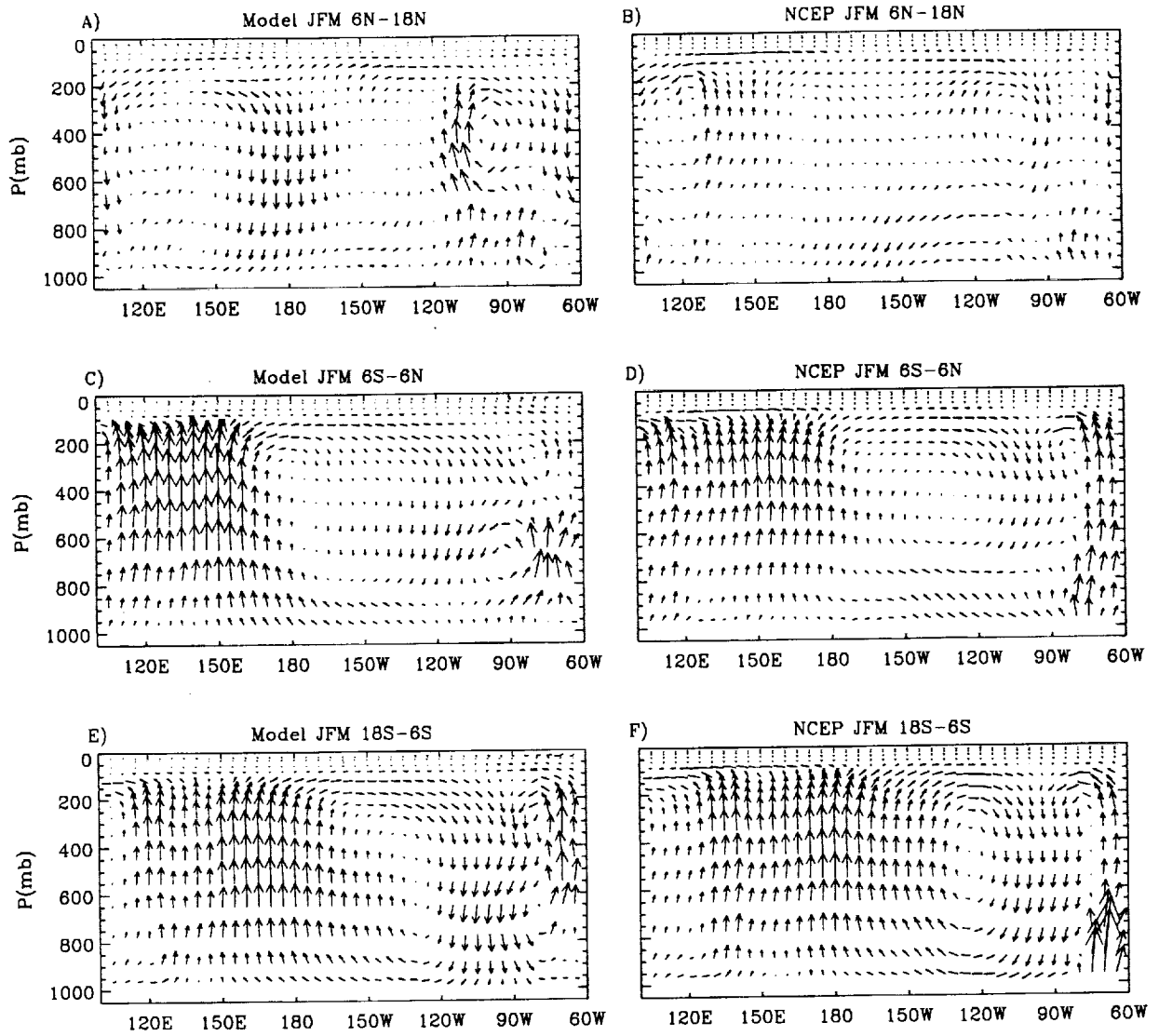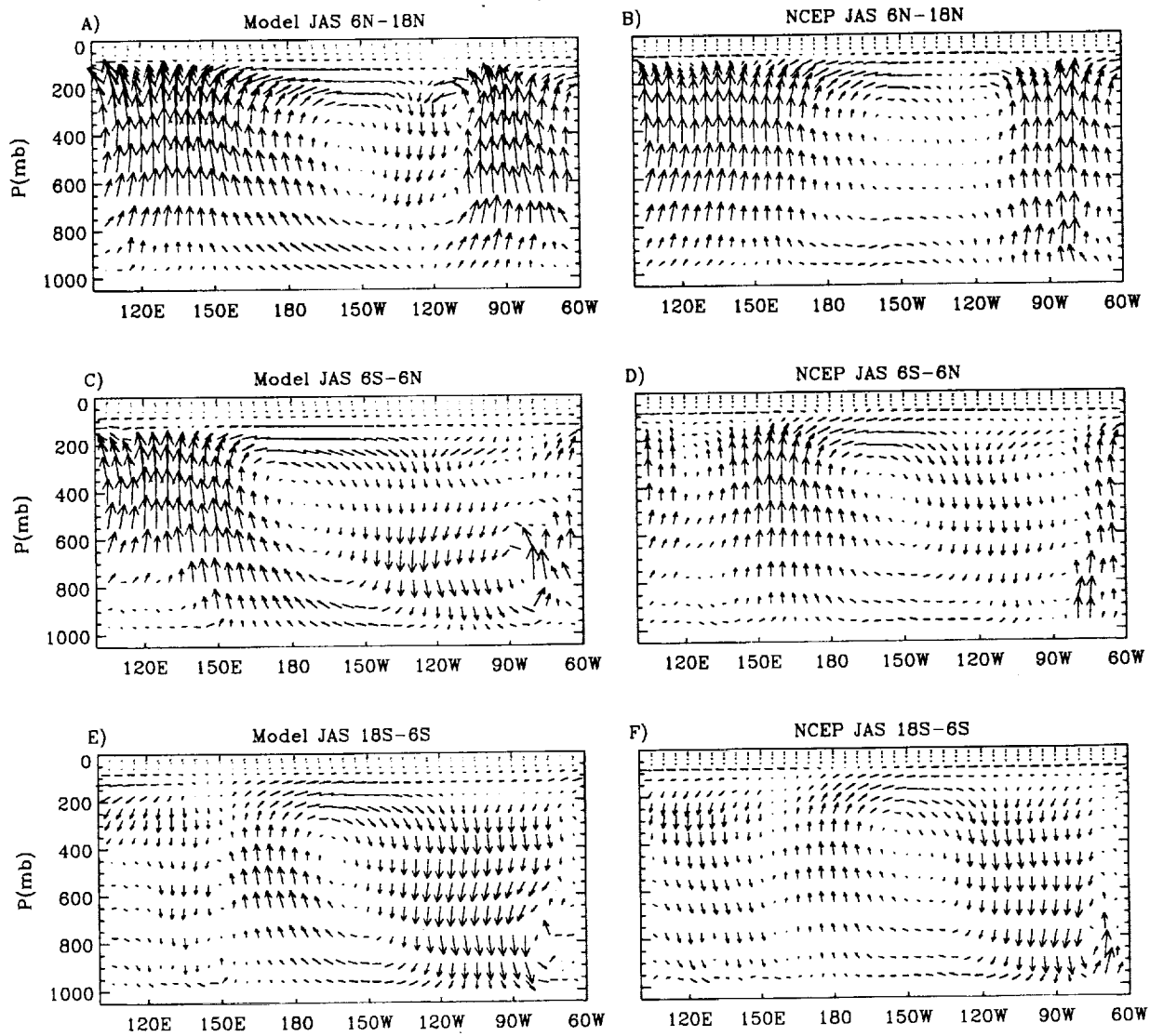
Figure 17: 1980-1999 Seasonal mean vectors of the divergent flow (u_χ, ω) in the longitude-pressure plane for JFM. Arrows show one time-step, forward trajectories $(\Delta\lambda, \Delta p) = (\cos\phi^{-1}u_\chi\Delta t, \omega\Delta t)$ where $\Delta t = 2.5$ days. Different panels show average circulation in three different 12° latitude bands: a) 18S-6S for the model; b) 18S-6S for the NCEP/NCAR re-analysis; c) 6S-6N for the model; c) 6S-6N for the re-analysis; c) 6N-18N for the model; and c) 6N-18N for the re-analysis.
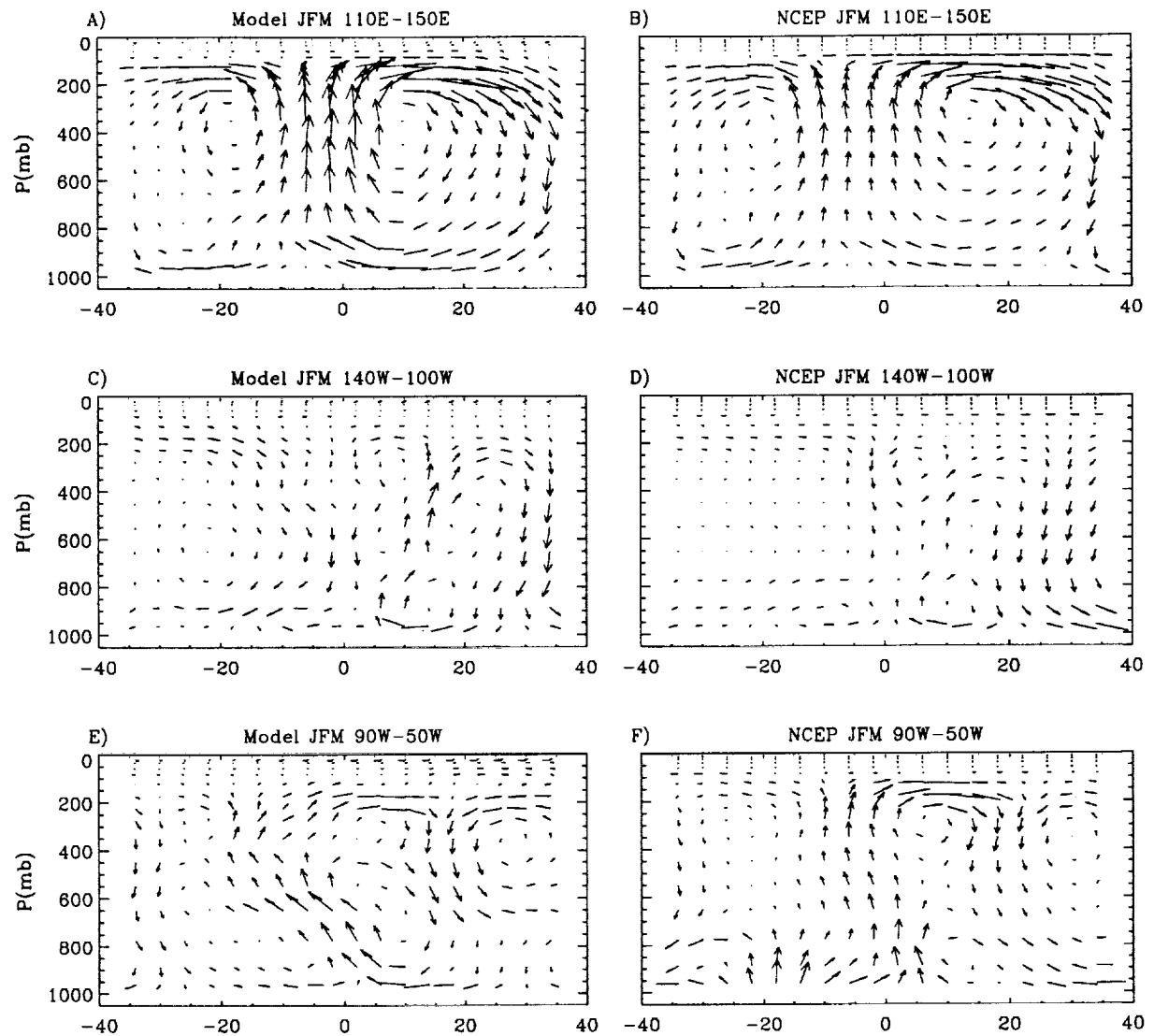
Figure 18: As in Figure 16 except for JAS.

Figure 19: 1980-1999 Seasonal mean vectors of the divergent flow (v_χ, ω) in the latitude-pressure plane for JFM. Arrows show one time-step, forward trajectories $(\Delta\phi, \Delta p) = (v_\chi \Delta t, \omega \Delta t)$ where $\Delta t = 2.5$ days. Different panels show average circulation in three different 40° longitude bands: a) 110E-150E for the model; b) 110E-150E for the NCEP/NCAR re-analysis; c) 140W-100W for the model; c) 140W-100W for the re-analysis; c) 90W-50W for the model; and c) 90W-50W for the re-analysis.
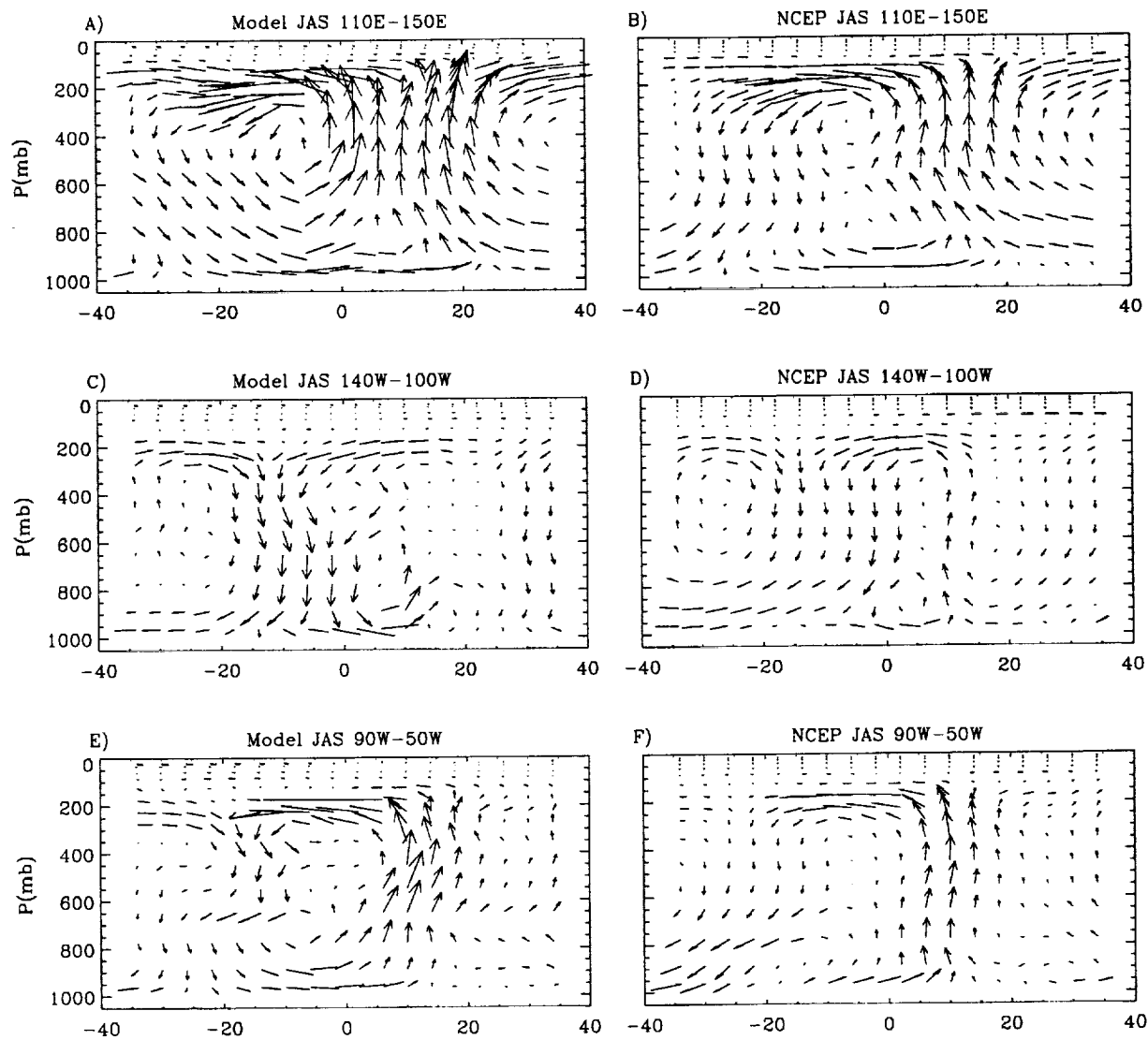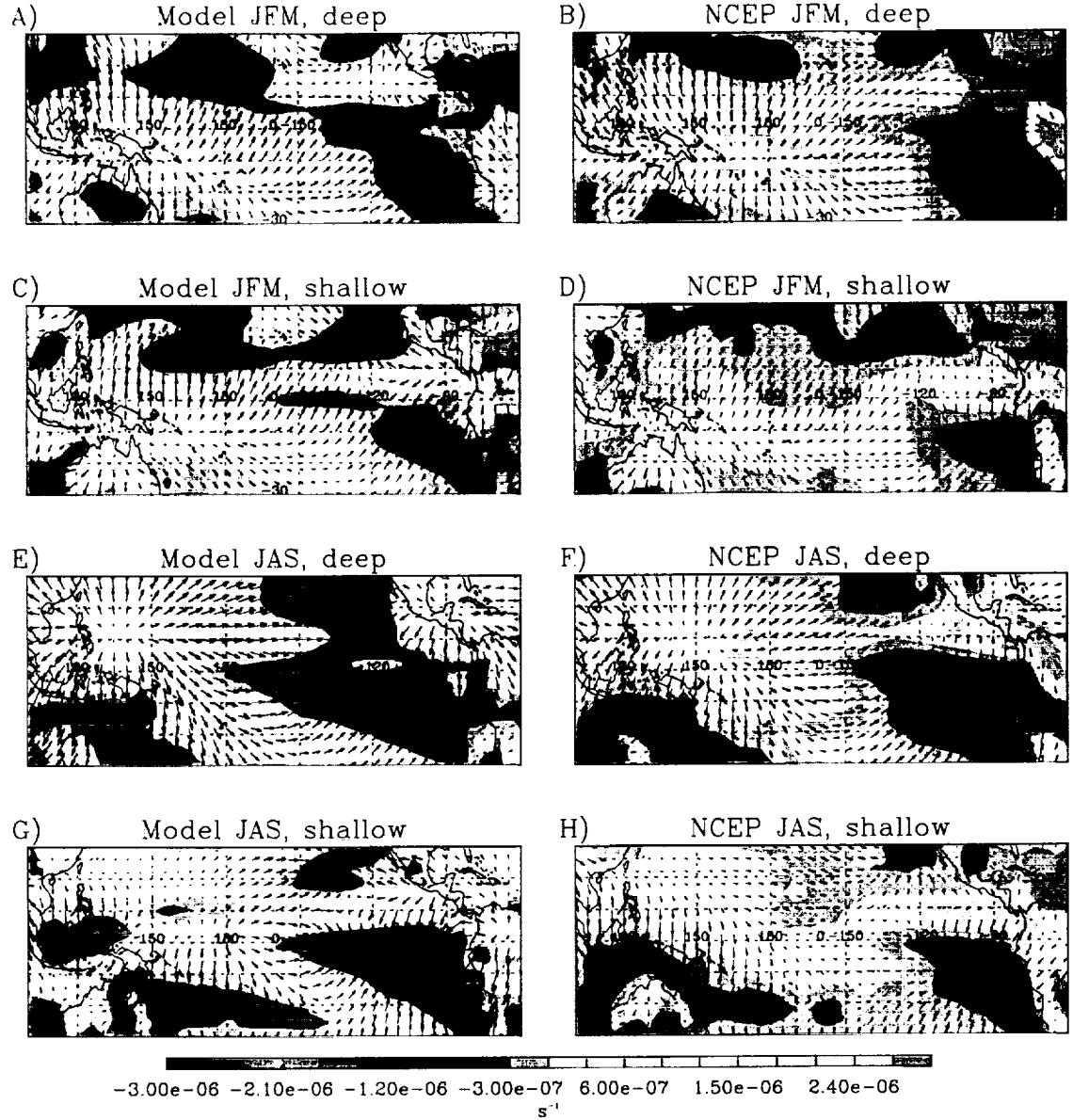
Figure 20: As in Figure 18 except for JAS.

Figure 21: 1980-1999 Seasonal-mean, horizontal structure of deep and shallow components of the divergent flow (see text) from the model and from the XCEP re-analysis. Arrows show one time-step, forward trajectories $(\Delta\lambda, \Delta\phi) = (\cos\phi^{-1}\widehat{u_\chi}^{s,d}\Delta t, \widehat{v_\chi}^{s,d}\Delta t)$ where we have used $\Delta t = 5.0$ days for the deep component and $\Delta t = 10.0$ days for the shallow component. Colored shading shows components of the divergence, $\widehat{\mathcal{D}}^{s,d}$, with an interval of 3×10^{-7} s^{-1} and a range indicated in the color bar at the lower edge of figure. Different panels show deep and shallow components for different seasons: a) JFM deep component for model; b) as (a) for XCEP/XCAR re-analysis; c) JFM shallow component for model; d) as (c) for re-analysis; e) JAS deep component for model; f) as (e) for re-analysis; g) JAS shallow component for model; h) as (g) for re-analysis.